Available online at www.sciencedirect.com

ScienceDirect

Nuclear Physics A 973 (2018) 116–148

NUCLEAR PHYSICS A

www.elsevier.com/locate/nuclphysa

Direct measurements of the lifetime of medium-heavy hypernuclei

(HKS (JLab E02-017) Collaboration)

X. Qiu [a], L. Tang [b,c,*], C. Chen [b], A. Margaryan [d], S.A. Wood [c], P. Achenbach [e], A. Ahmidouch [f], I. Albayrak [p], D. Androic [g], A. Asaturyan [d], R. Asaturyan [1], O. Ates [b], R. Badui [h], P. Baturin [h], W. Boeglin [h], J. Bono [h], E. Brash [i], P. Carter [i], X. Chen [a], A. Chiba [j], M.E. Christy [b], M.M. Dalton [k,c], S. Danagoulian [f], R. De Leo [l], D. Doi [j], M. Elaasar [m], R. Ent [c], H. Fenker [c], Y. Fujii [j], M. Furic [g], M. Gabrielyan [h], L. Gan [n], F. Garibaldi [o], D. Gaskell [c], A. Gasparian [f], T. Gogami [j], O. Hashimoto [1], T. Horn [c], B. Hu [a], Ed V. Hungerford [p], M. Jones [c], H. Kanda [j], M. Kaneta [j], D. Kawama [j], H. Khanal [h], M. Kohl [b], A. Liyanage [b], W. Luo [a], K. Maeda [j], P. Markowitz [h], G. Marikyan [d], T. Maruta [j], A. Matsumura [j], V. Maxwell [c], A. Mkrtchyan [d], H. Mkrtchyan [d], S. Nagao [j], S.N. Nakamura [j], A. Narayan [q], C. Neville [h], G. Niculescu [r], M.I. Niculescu [r], A. Nunez [h], Nuruzzaman [q], Y. Okayasu [j], T. Petkovic [g], J. Pochodzalla [e], J. Reinhold [h], V.M. Rodriguez [s], C. Samanta [t], B. Sawatzky [c], T. Seva [g], A. Shichijo [j], V. Tadevosyan [d], N. Taniya [j], K. Tsukada [j], M. Veilleux [i], W. Vulcan [c], F.R. Wesselmann [u], T. Yamamoto [j], Z. Ye [b], K. Yokota [j], L. Yuan [b], S. Zhamkochyan [d], L. Zhu [b]

[a] *School of Nuclear Science and Technology, Lanzhou University, Lanzhou, Gansu, 730000, China*
[b] *Department of Physics, Hampton University, VA 23668, USA*
[c] *Thomas Jefferson National Accelerator Facility, Newport News, VA 23606, USA*
[d] *Yerevan Physics Institute, Yerevan 0036, Armenia*
[e] *Institute für Kernphysik, Johannes Gutenberg-Universität Mainz, D-55099 Mainz, Germany*
[f] *Department of Physics, North Carolina A&T State University, Greensboro, NC 27411, USA*
[g] *Department of Physics & Department of Applied Physics, University of Zagreb, HR-10000 Zagreb, Croatia*
[h] *Department of Physics, Florida International University, Miami, FL 33199, USA*
[i] *Department of Physics, Christopher Newport University, Newport News, VA 23606, USA*
[j] *Graduate School of Science, Tohoku University, Sendai, Miyagi 980-8578, Japan*

https://doi.org/10.1016/j.nuclphysa.2018.03.001
0375-9474/

[k] *University of Virginia, Charlotesville, VA 22904, USA*
[l] *Istituto Nazionale di Fisica Nucleare, Sezione di Bari and University of Bari, I-70126 Bari, Italy*
[m] *Department of Physics, Southern University at New Orleans, New Orleans, LA 70126, USA*
[n] *Department of Physics, University of North Carolina Wilmington, Wilmington, NC 28403, USA*
[o] *INFN, Sezione Sanità and Istituto Superiore di Sanità, 00161 Rome, Italy*
[p] *Department of Physics, University of Houston, Houston, TX 77204, USA*
[q] *Mississippi State University, Mississippi State, MS 39762, USA*
[r] *Department of Physics, James Madison University, Harrisonburg, VA 22807, USA*
[s] *Escuela de Ciencias y Tecnologia, Universidad Metropolitana, San Juan, Puerto Rico*
[t] *Department of Physics & Astronomy, Virginia Military Institute, Lexington, VA 24450, USA*
[u] *Department of Physics, Xavier University of Louisiana, New Orleans, LA, USA*

Received 29 December 2017; received in revised form 20 February 2018; accepted 4 March 2018
Available online 8 March 2018

Abstract

The lifetime of a Λ particle embedded in a nucleus (hypernucleus) decreases from that of free Λ decay mainly due to the opening of the $\Lambda N \to NN$ weak decay channel. However, it is generally believed that the lifetime of a hypernucleus attains a constant value (saturation) for medium to heavy hypernuclear masses, yet this hypothesis has been difficult to verify. This paper presents a direct measurement of the lifetime of medium-heavy hypernuclei that were hyper-fragments produced by fission or break-up from heavy hypernuclei initially produced with a 2.34 GeV photon-beam incident on thin Fe, Cu, Ag, and Bi target foils. For each event, fragments were detected in coincident pairs by a low-pressure multi-wire proportional chamber system. The lifetime was extracted from decay time spectrum formed by the difference of the time zeros between the pairs. The measured lifetime from each target is actually a statistical average over a range of mass with mean about 1/2 of the target mass and appears to be a constant of about 200 ps. Although this result cannot exclude unexpected shorter or longer lifetimes for some specific hypernuclei or hypernuclear states, it shows that a systematic decrease in lifetime as hypernuclear mass increases is not a general feature for hypernuclei with mean mass up to $A \approx 130$. On the other hand, the success of this experiment and its technique shows that the time delayed fissions observed and used by all the lifetime measurements done so far on heavy hypernuclei could likely have originated from hyper-fragments lighter than the assumed masses.

Keywords: Hypernuclei; Lifetime; Fragment; Hyper-fragment; Weak decay

1. Introduction

The Λ hypernucleus was discovered in an emulsion experiment in 1952 [1,2]. Since then, there have been extensive investigations of Λ hypernuclei, using various reactions and detection methods, to study the ΛN interactions (strong or weak) as well as the role of the Λ in the nuclear medium. These have illuminated hypernuclear spectroscopy, branching ratios, and decays.

* Corresponding author at: Department of Physics, Hampton University, VA 23668, USA.
E-mail address: tangl@jlab.org (L. Tang).
[1] Deceased.

In the weak interaction regime, a free Λ decays weakly via a mesonic channel into a nucleon and a pion, with a lifetime of 263.2 ± 2.0 ps [3]. However, the lifetime of a Λ particle embedded in a hypernucleus is significantly shorter, because of opening of other channels within the nuclear environment. Thus, in the nucleus, the Λ has the possibility of decaying via the weak interactions mainly through;

$$\Lambda \rightarrow N\pi \ (+37 \text{ MeV}) \text{ or } \Lambda N \rightarrow NN \ (+176 \text{ MeV}). \tag{1}$$

The lifetime is sufficient for the Λ particle to transition to the lowest shell, $1S$, in the effective nuclear potential well, as it remains an identifiable particle in the nuclear environment. On the other hand, Pauli exclusion inhibits the decay to πN [4] as the recoiling nucleon must have sufficient energy to enter an unfilled nuclear shell. Thus decaying to NN becomes dominant for hypernuclei beyond the $1S$ shell since, for these cases, the recoiling nucleons have sufficient energy to leave the nucleus.

One unique feature of ΛN interactions in the nuclear medium is their short range, initially discussed by Primakoff and Chesterton [5] and more extensively discussed by recent reviews based on up-to-date investigations [6,7]. This is essentially a result of the large energy and momentum transfers required for the inelastic $\Lambda N \rightarrow NN$ reaction in a nucleus. Thus one expects the hypernuclear lifetime to reach a constant value (saturation) when medium to heavy hypernuclear masses are reached. The dominant two-body channels for this decay includes both proton ($\Lambda p \rightarrow np$) and neutron stimulated ($\Lambda n \rightarrow nn$) decays, but there are also a smaller contributions from three body decays, i.e. $\Lambda NN \rightarrow nNN$ (+176 MeV), in which the Λ particle interacts with a correlated nucleon pair. One would also naturally expect that there is a limit on the nucleon pairs accessible by the Λ particle due to its limited interaction range. Therefore, the lifetime is expected to "saturate" in heavier hypernuclei with the $1P$ shell fully filled and beyond. However, experimental verification of this behavior, particularly with precise lifetime measurement on heavy hypernuclei, has been difficult.

Early results were obtained for light hypernuclei, $A \leq 5$, using an emulsion technique with rather limited precision [8–12]. The lifetimes of ${}^{4}_{\Lambda}$H, ${}^{4}_{\Lambda}$He, and ${}^{5}_{\Lambda}$He were later measured with improved precision, using counting techniques [13–16], and the lifetimes of p-shell Λ hypernuclei, ${}^{9}_{\Lambda}$Be, ${}^{11}_{\Lambda}$B and ${}^{12}_{\Lambda}$C have also been measured [16]. Overall, the results indicate a quick decrease from a lifetime approximately equal to that of a free Λ to a lifetime of approximately 200 ps in p-shell hypernuclei.

Lifetime measurements for heavier hypernuclei using emulsion techniques are even more difficult due to the decrease with A in production yield. An early attempt to measure the lifetime of a heavier p-shell hypernuclei used relativistic ^{16}O ion beam incident on a polyethylene target. Although, the actual hypernuclei were not determined [17], they were assumed to be mass 16 hypernuclei. The basic technique was a decay range measurement and the lifetime was reported as 86 ps with a systematic error quoted to be about ± 30 ps. In spite of the contradictory result, the experiment was the first to use the counter-type technique to measure the decay range.

A later counter-type of experiment at KEK using the (π^+, K^+) reaction [18] accompanied by Λ weak decay positively identified the hypernuclei from the ground state (as well as low-lying excited states in case of a heavy target). Using the time-of-flight (TOF) technique and a production reference time, the experiment measured directly the decay time spectra of ${}^{11}_{\Lambda}$B, ${}^{12}_{\Lambda}$C, ${}^{27}_{\Lambda}$Al, ${}^{28}_{\Lambda}$Si, and ${}^{56}_{\Lambda}$Fe. With such a combination of identification of hypernuclei and direct decay time measurement, its result was obviously the most reliable one. The measured lifetimes were approximately constant, $\sim 210 \pm 20$ ps, indicating a saturation of hypernuclear lifetime as $A > 12$. While successful, it would be difficult to apply this technique to measure the lifetimes of heavier hypernuclei as the production yield of low-lying hypernuclei decreases significantly as A further increases.

In the last few decades, theoretical studies of two-body and three-body decay widths have increased in sophistication [19–21]. Two recent accurate theoretical calculations of lifetimes of Λ hypernuclei over the full mass range (up to A = 209) both predicted a constant saturation value around 200 ps [22,23].

The technique of delayed fission with the recoil shadow method to measure lifetime of heavy hypernuclei was first applied by experiments at CERN with a $\overline{p}$ beam [24]. The time delayed fission was interpreted as being induced by the large energy released from non-mesonic weak decay of hypernuclei with masses in the vicinity of target nuclei (Bi and U). While the lifetime of hypernuclei in the region of Bi was reported to be 250^{+250}_{100} ps, a rather short lifetime of 125 ± 15 ps was claimed for those in the region of U. Later, the COSY-13 collaboration applied a similar technique but with a 1.5 GeV proton beam incident on Au, Bi, and U targets [25–27]. It was hoped that an increased momentum transfer to hypernuclei would enhance their decay range and thus improve the uncertainty of measurement.

The technique was to determine the lifetime of the recoils from the targets by measuring the distance that the projectiles traveled out of target due to large momentum transfer before decaying into fission fragments. Such a recoil distance measurement was achieved by a planar fission fragment detection system that was located away from and parallel to the beam. Without identifying the recoiled projectiles, the fission fragments that reached the "shadow" region were considered to be from time delayed fission decays induced by hypernuclear non-mesonic decay. The COSY experiment aimed to resolve the conflicting results from early CERN experiments. The fitted lifetime was reported as 145 ps averaged over a mass range of $180 < A < 225$, considering only few nucleons might be evaporated before final weak decay. With this method, the lifetime is indirectly measured and depends strongly on theoretical models that describe the time evolution of the system during the reaction, i.e. transporting calculations for the initial fast non-equilibrium phase and statistical calculations for the final evaporation phase.

Such significantly shorter lifetime for heavy Λ hypernuclei reported by these experiments is puzzling. If correct, the result obviously contradicts the expected saturation of the lifetime and could not be explained by the existing theories on weak baryonic interactions taken place in nuclear medium, although there are theoretical efforts in attempt to explain such a decreasing feature without violating the $\Delta I = 1/2$ rule.

Λ-hypernuclei have been extensively studied at JLab with the high quality CEBAF electron beam using the $(e, e'K^+)$ reaction. A lifetime experiment was also carried out with a specially designed fission fragment detector (FFD) and experimental technique. Although no mass or hypernuclear states were identified (similar to the prior CERN and COSY experiments), the experiment allowed clear recognition of the source of decay process that gives the time delayed fission. It measured the decay time spectrum which provided a direct lifetime measurement, minimizing systematic error which may come from techniques using the range method.

In the Section 2, the origin of delayed fission is discussed from the points of view of the production mechanisms of hypernuclei, characteristics and populations of hypernuclear structures, and decays of hypernuclei from different excitation levels. Experimentally obtained hypernuclear mass (or Λ binding energy) spectroscopies from electro-production are used as examples to justify the clarification of the sources of the delayed fissions. These considerations are rather different than from early CERN and COSY experiments and they defined the applied technique and analysis method of the JLab experiment. The experimental technique and its apparatus are discussed in detail in Section 3. Characteristics of the basic data, required calibrations and reconstruction procedures are presented in Section 4. The decay time analysis is discussed in Section 5. A simulation that verified that stopped decays inside targets due to energy loss are responsible for the linear distribution in the logarithm decay time spectrum is also presented. In Section 6, the method of fitting lifetime from the decay time spectrum that composes multiple contributions as well as event mixing is presented. In Section 7, the measured lifetime and important observations from this experiment are discussed. The conclusion is given in Section 8.

2. Experimental consideration

The lifetime experiment (JLab E02-017) which took place in Hall C at Jefferson Laboratory, ran parasitically to the HKS hypernuclear mass spectroscopy experiment using the $(e, e'K^+)$ reaction [28]. The experiment was installed behind the spectroscopy experiment, in front of the photon-dump, and used the bremsstrahlung photon-beam produced from the spectroscopy target as the radiator. The photon-beam had a narrow angular distribution peaking at zero degrees, with a bremsstrahlung energy spectrum up to 2.34 GeV. The energy threshold required to photo-produce a Λ particle is about 700 MeV. Fission fragments from decays with time delay were the sources to study the lifetime of hypernuclei.

However, without identification of hypernuclear production, the first important challenge one faces is the identity of the decayed hypernuclei since it could be the major source of systematic error of experimental methods. The features of electro- or photo-production mechanisms can provide useful clues about the produced hypernuclei as well as their decays. With photon energies ranging from 0.7 to 2.34 GeV, photo-production is peaked in the forward direction, i.e. the positively charged koan from the $(e, e'K^+)$ reaction is emitted within a small forward angle and takes most of the momentum. Still, the 3-momentum transfer to the produced Λ particle is significant, $\mathbf{q} \geq 350$ MeV/c. While such a large momentum transfer significantly reduces the production cross section of low-lying hypernuclear states, the advantage is that the Λ particle converted from a proton at the outer orbital state can drop to an inner orbit when coupled back to the core, producing a hypernucleus in a deeply bound state.

Full mass spectroscopies of several light to medium heavy hypernuclei were observed using the $(e, e'K^+)$ reaction by the HKS experiment in front of this lifetime experiment. For example, Fig. 1 illustrates the spectrum (in terms of Λ binding energy) of the $^{12}_{\Lambda}$B hypernucleus obtained from a ^{12}C target. The full spectrum can be separated into two distinct regions, i.e. the regions of low-lying discrete states and high-lying continuum. The high-lying region is commonly referred as the quasi-free region.

The focus of most hypernuclear studies is the region of low-lying states with a Λ binding energy from the ground state to approximately about $+10$ MeV above threshold. To produce such low-lying hypernuclear states, the Λ particle must be converted from one of the outermost a few protons and the core nucleus is at the ground state or a low-lying excited states. Taking advantage of large momentum transfer, the Λ particle can transition to a lower orbital state and then couple back to the core.

Hypernuclei in the ground state (or an isomeric state) can only decay weakly, primarily with a non-mesonic decay mode. Hypernuclei in low-lying excited states can cascade down to the ground state by electromagnetic decay(s) with γ emission and then decay weakly. The time for EM decay is negligible compared to that for weak decay. With an excitation energy above the nucleon emission threshold, a low-lying hypernucleus can also decay strongly by nucleon emission with the residual becoming a lighter but more stable hypernucleus. This lighter hypernucleus then decays weakly from its ground state. Hypernuclei from this mass region can be referred as

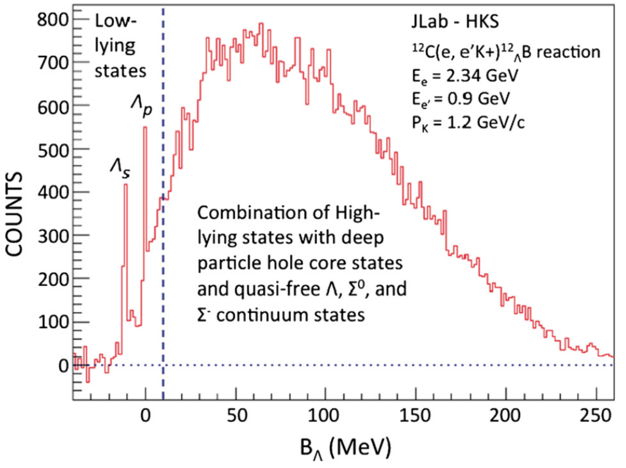

Fig. 1. The accidental background subtracted full missing mass spectrum in terms of Λ binding energy of ${}^{12}_{\Lambda}$B hypernucleus. The detailed spectroscopy in the region of low-lying states with a Λ in s and p shells was published [30].

"cold" hypernuclei. Obviously, measurement of lifetime of heavy hypernuclei at or close to the target mass must be made by the events from the decay of "cold" hypernuclei.

Hypernuclei with binding energies $B_\Lambda > +10$ MeV form the so called quasi-free mass distribution. However, they are simply made of single Λ in the continuum states since no experiment had ever shown a free Λ lifetime from events selected from this mass region. In fact, hypernuclei in this mass region are in high-lying states which are formed by the Λ particle converted from protons at inner states so that the core nuclei are highly excited. Such "hot" hypernuclei should then be interpreted as coupling of Λ particle at various accessible orbital states to highly excited nuclear cores at various deep particle–hole states. They are extremely unstable and decay primarily by strong break-up or fission. Therefore, they are the sources of hyper-fragment production, i.e. a Λ particle actually coupling with one of the fission fragments. The hyper-fragments are formed instantaneously and thus are impossible to identify without a mass determination technique.

As shown in Fig. 1, the amount of "cold" hypernuclei is only a small fraction of the overall hypernuclear production. It is about 5.6% in case of ${}^{12}_{\Lambda}$B electro- or photo-production. Fig. 2 shows this ratio measured for ${}^{7}_{\Lambda}$He [34], ${}^{9}_{\Lambda}$Li, ${}^{10}_{\Lambda}$Be [35], ${}^{12}_{\Lambda}$B, ${}^{28}_{\Lambda}$Al and ${}^{52}_{\Lambda}$V [36]. Among these, ${}^{7}_{\Lambda}$He is the lightest p-shell hypernucleus and its "cold" hypernucleus ratio is as small as only about 2%. As the mass A increases, additional low-lying orbital states become available and the ratio increases quickly. However, the increase of this ratio slows down beyond p-shell due to a rising competition of a available deep particle–hole states plus higher orbital states of Λ particle. The solid line in the figure is a fit using 3rd order polynomials over all the points, while the dotted line is just a straight line fit using only the last three points from ${}^{12}_{\Lambda}$B, ${}^{28}_{\Lambda}$Al, and ${}^{52}_{\Lambda}$V. These simple fits are only to illustrate a general tendency of the ratio as mass A increases. In fact, starting from medium heavy mass, this ratio is likely to decrease or saturate as function of A and should not exceed about 10%.

The above consideration raises a technical challenge to the lifetime measurement of heavy hypernuclei since none of the existing experiments had effective method to single out the events from "cold" hypernuclei while the hyper-fragments decaying from "hot" hypernuclei are expected to play the major role. Since fragmentation takes no time, hyper-fragments should be

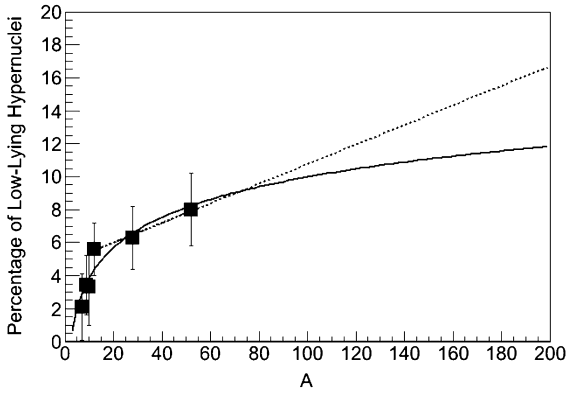

Fig. 2. The ratio of low-lying hypernuclei to overall production from electro-production with the 3-momentum transfer **q** to the converted Λ particle at $\sim$350 MeV/c. The data points are from the JLab HKS experiments on ${}^{7}_{\Lambda}$He, ${}^{9}_{\Lambda}$Li, ${}^{10}_{\Lambda}$Be, ${}^{12}_{\Lambda}$B, ${}^{28}_{\Lambda}$Al, and ${}^{52}_{\Lambda}$V hypernuclei. The solid and dotted lines are simple fits only for illustration of the general character of A dependence.

produced instantaneously and fly out of target in range type of measurements just like the "cold" hypernuclei, except that their emissions have wide angular distribution. These could cause major systematic errors in all the previous experiments.

Although the JLab experiment cannot make an event selection on "cold" hypernuclei also, it was designed to detect a time-coincident pair of fragments with independent time zero reconstructions, so that the events from weak decay of hyper-fragments could be unambiguously identified. Secondly, it attempted to make direct decay time measurement to avoid systematic errors from momentum (or mass) assumptions of the delayed decay products.

3. Experimental technique

As mentioned in Introduction, this experiment ran parasitically to the HKS experiment which had the priority on beam time and schedule. To maximize the bremsstrahlung beam profile, the apparatus (FFD) of this experiment together with the photon dump were arranged 15 m downstream (the largest allowable distance by the experimental hall) of the HKS target which was used as the radiator. To shield against high radiation backgrounds for this experiment as well as protecting the HKS spectrometers, this combined system was completely and heavily shielded by a bunker built by concrete and ion blocks. Due to the HKS priority, high radiation levels and the extended time needed for experimental modification, it was not possible for this experiment to make configuration changes during the scheduled beam time.

3.1. Fission fragment detector

A specially developed fission fragment detector (FFD) [29] was used to detect pairs of fragments from either photo-induced fission or the weak decay of a heavy hypernuclei (see Fig. 3). Similar to all previous experiments studying the lifetime of heavy hypernuclei, the production and mass of hypernuclei were not tagged and the existence of hypernuclei was inferred from the observation of a long $\sim$200 ps decay time spectrum.

As shown in Fig. 3, the FFD consists of four multi-wire proportional chamber (LPMWPC) units, operated at low gas pressure, $\sim 1-3$ Torr, which makes the response time short enough for

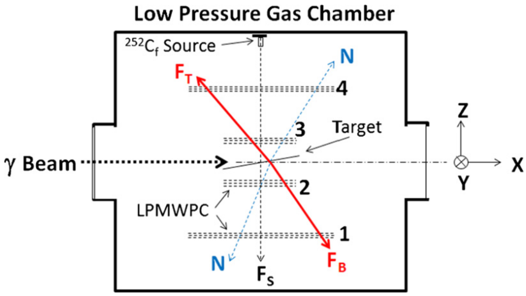

Fig. 3. Schematic illustration of the FFD and the experimental concept. FT and FB are a pair of fragments detected in coincidence by the two TOF arms; F_S is a fragment from a fission source used for calibration; and N's are missing nucleons from fission or break up.

timing purposes. The low pressure also makes the detector insensitive to nucleons and light ions (with $Z < \sim 6$) because a large initial ionization is required to make a signal. Furthermore, it also minimizes energy loss, allowing fragments with high Z to travel through the paired LPMWPC units.

The four units are mounted in parallel to the $X - Y$ plane with fixed Z coordinates, $Z = \pm 3$ cm (± 10 cm) for the inner (outer) planes, symmetrically. They form two TOF (Top and Bottom) arms, above and below the beam (along X axis). Each unit has one anode plane sandwiched by two cathode planes. The anode signal is used to measure the time with respect to the reference time (set by the anode signal from the Unit 1 – the outer unit at the bottom). The time difference between the pair of inner and outer units provides the absolute TOF measurement. A coincidence between the two TOF pairs was used to select events that had a fragment detected by each pair. A TOF range ($\sim$10 ns) gate was applied which was based on the possible range of velocities the induced fission fragments.

The anode signal (a pulsed charge collection at a specific position) has corresponding induced signals on the two cathode planes. They provide the position measurement in the X and Y directions with the wire orientations of the two cathode planes normal to each other. Using a digital delay line technique, an induced signal at a given location (X or Y) on the cathode plane splits and is transmitted to the Left (L) and Right (R) through the remaining chain of delay lines. The times of these two signals are measured in reference to that of the anode signal, so that the two cathode times are uniquely correlated but are not affected by the TOF variations. With a constant total delay time of the delay line chain, the sum of the L and R times is thus constant in case of single fragment hit. Position is determined by the difference of the L and R times. By gating on the sum of the L and R times for each cathode, events that had only two fragments, one detected in each TOF arm were selected. Detailed discussions on the design, performance, source calibration and characteristics of this FFD can be found in Ref. [29].

3.2. Targets

The targets were constructed by depositing strips (in the Y direction) of thin Fe, Cu, Ag, (Au), Bi and (U) film coatings, with natural isotopic abundance, onto a single 12.0 μm thick aluminized mylar foil, 134.5 mm long and 50 mm wide. Table 1 lists the deposited materials, approximate thicknesses, strip widths and separations measured after the depositions were made. Due to the difficulty in masking the foil, the actual separations between strips varied and none reached the desired width of 2.5 mm. The main difficulty is that the thin mylar backing can be easily damaged

Table 1
Target materials and strip configuration.

Target	Thickness (μm)	Width (mm)	Separation (mm)
Au	0.4	29.0	
			0.0
Cu	0.8	25.5	
			2.0
Fe	0.8	20.0	
			1.0
Ag	0.8	21.5	
			1.0
Bi	0.4	20.0	
			1.5
$U_{natural}$	< 0.003	11.5	

when the temperature exceeds ∼90 °C. The hot spotting source needed to be far away from foil to avoid overheating and therefore the growing process took weeks for each material. Before experiment started, only one such foil with five of the six required materials was made although it did not fully meet the experimental requirements. Due to another technical error, the U material was not successfully diffused onto the backing (since U cannot be spotted).

The target foil was positioned between the two TOF arms and inclined at an angle of 8° to the beam (as shown in Fig. 3, with the strips in sequence along the beam direction. Such an arrangement minimizes the energy loss for the outgoing fragments toward the MWPC pairs while maximizing the target thickness in the beam direction for production yield. The bremsstrahlung beam spread allows multiple target strips to be hit by photons simultaneously.

The Fe and Ag targets were arranged at or near the center of the bremsstrahlung beam while the Cu and Bi targets were in the beam halo. Such an arrangement was based on two general considerations. First, the lifetime of "cold" hypernuclei from Fe was reliably measured by the KEK experiment. A measurement from the Fe target by this experiment with similar or better statistical uncertainty was considered to be an important technical verification. Secondly, although the yield (combining the overall cross section and target thickness) of hypernuclei is significantly smaller from Bi than that from Fe, it is known from beam induced fission that the fission probability of Bi is more than two to three orders of magnitude higher than of Fe. Thus, a much lower event yield from Fe was expected when designing this experiment, if fission associated with hypernuclei is mainly from non-mesonic weak decay and the fission decay rate of "hot" hypernuclei is not high. Therefore, positioning the Fe target to be at/near the center was to achieve more even event rates from these targets. However the results were unexpected and they showed a high production rate of hyper-fragments from fission decay of "hot" hypernuclei (more discussions in later sections). Due to the existence of only one target foil at run time and the difficulty to quickly make more target foils, it was impossible to make a configuration change for target optimization during the experiment.

Since the photons radiating from the thin HKS targets were sharply peaked at zero degrees, only the Fe, Cu, Ag and Bi targets were covered by the beam profile. Thus there were no useful data obtained from the Au and U targets on the edges. Furthermore, the insufficient gaps between target materials with the achievable resolution on fission position caused mixing of events between adjacent targets. Thus analyses of mixing and multiple lifetime fitting were required (to be discussed later).

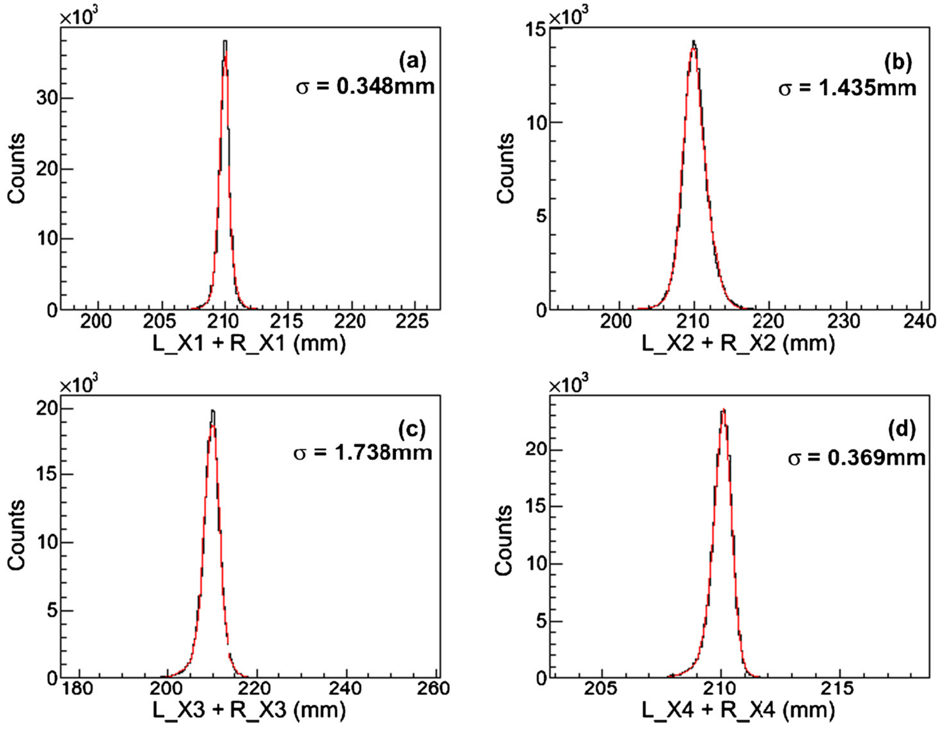

Fig. 4. The L and R sum in length unit for the four X coordinate measurements. The active outer plane size is 210×210 mm^2 ((a) and (d)) while that of the inner planes ((b) and (c) is 105×105 mm^2). The inner planes which are very close to the target surface had poorer position resolution due to the influence of pile-up charges (low energy electrons) emitted from target materials.

3.3. Position determination and resolution

The single plane position resolution depends on the precision of the induced L and R time signals. By referencing to their anode time, the time precision is mainly affected by the large signal size variation due to broad ranges of fragment mass and Z. Thus, the correlations of the anode signal size with respect to the L and R times were studied and corrections as functions of the anode signal size were applied. The L and R sum (i.e. the plane size) and the position range from the L and R difference were used as calibration gauges. These analysis procedures optimized the position resolution for each measured position coordinate. The mean and σ width of the L and R sum, converted to length units (mm) by the calibrated time-length conversion factor, represents the full size of the coordinate plane and the position resolution (see Fig. 4).

Although the low pressure FFD in principle detects only nuclear fragments with high Z, its detection efficiency can be influenced by pileup charge from low energy ($\sim$10 keV) atomic electrons induced by beam reactions with the target foil. The charge reduces the potential between the anode and cathodes of the MWPC units which share a common low pressure gas with the target foil. This pileup was particularly severe for the two inner units (with an active area of 100×100 mm^2) that are only 3 cm away from the beam central axis. Their signal size was significantly reduced, increasing the time measurement uncertainty. As shown by Fig. 4, the position resolutions of the inner units (#2 and #3) were only about 1.44 and 1.74 mm, respectively,

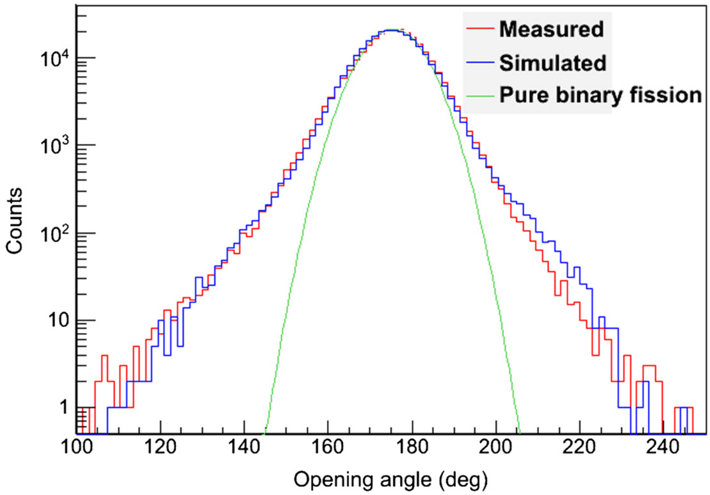

Fig. 5. Distributions of the opening angles between the two detected fragments. Histogram in red is from real data while the simulation is in blue. (For interpretation of the colors in the figure(s), the reader is referred to the web version of this article.)

which dominated the precision of the reconstructed fission position projected in the beam direction (X-axis). For the inner planes, the resolution is about 15 times worse than observed for tests with a fission source [29], while it is about three times worse for the outer planes. Thus, the effect of pile-up charge had a strong influence on the position resolution. In addition, the actual beam centroid was shifted up (in Z direction) by about 1.5 mm. This shift resulted in a better event rate from the Bi target. However, it caused higher charge pile-up on the two planes (#3 and #4) above the beam axis so that their position resolutions were worse than those of the two planes below the beam. In addition, this small beam axis shift put the Au target region almost completely outside the beam profile.

The reconstruction resolution for the fission positions on the target foil was dominated by that of inner units due to charge pile-up. The level of this influence could not be fully realized before a full offline analysis with all necessary corrections were completed. Therefore, it was not possible during the experiment to realize a further optimization by a FFD configuration change.

4. Characteristics of measurements

4.1. Opening angle of the two detected fragments

For each detected fragment, its emission trajectory was determined by the two positions measured by the associated TOF pair of MWPC units. The origin of the trajectory was defined by its intersection with the known target foil plane, under the assumption that the fission took place in the target foil. Since each event required two coincidentally detected fragments, one from each TOF pair, the fission position on the target foil was then defined by the average of the two origins. Using this fission position on the target and the two measured positions on the MWPC units, the trajectory of each fragment was then refit and the opening angle between the two trajectories was calculated. The histogram in red color in Fig. 5 shows the distribution of the measured opening angles between the two fragments detected in coincidence. The mean is $\sim$175.6° (due to

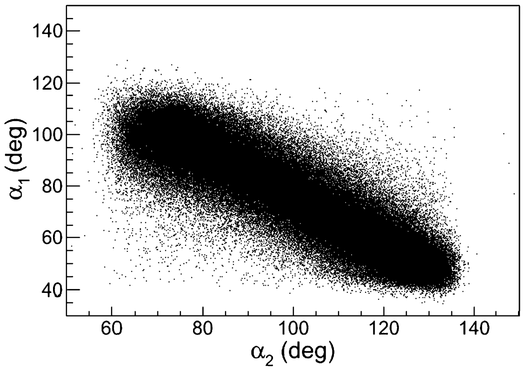

Fig. 6. Correlation of the emission angles measured with respect to the beam axis between the two detected fragments. The density of the distribution represents the probability.

forward boost in beam direction). Using the assumption of pure and prompt binary fission with a momentum range from 200 to 800 MeV/c and taking into account the position resolutions, the opening angle distribution was simulated by a Monte Carlo with an assumed primary mass (Fig. 5). In one step binary fission mode, the two fragments are correlated and thus the distribution should be narrower (σ ∼6.5°). However, this well-defined correlation can be lost if either multiple fragments are emitted or there exist obviously events from two-step process (see later discussions).

Fig. 6 shows the measured correlation between the two fragment emission angles with respect to the beam. The broadened width of this correlation was due to events that had the two fragments emitted without back-to-back correlation, i.e. the extended tail seen in Fig. 5. Using the measured angle correlation and probability (density distribution), simulated events were generated and their opening angle distribution is shown as the histogram in blue in Fig. 5. These simulated events with known fission positions were then used to extract the photon beam profile and to estimate the event-mixing ratio between adjacent target regions (see later discussion).

4.2. *Observed fission processes*

Based on the previously discussed consideration on the decay of "cold" and "hot" hypernuclei, the two fragments detected in coincidence by the two TOF arms are expected to originate from two types of fission or decay processes, i.e. one- and two-step decays as illustrated by Fig. 7.

For one-step decay, both of the two detected decay fragments are from a single fission process. Thus there should be two contributing sources. One is the beam induced fission or nuclear break-up. Since the reaction time is extremely short, both fragments have "prompt" decay times with respect to the reaction time. The second is a fission induced by non-mesonic weak decay (with a release energy of 176 MeV) of a "cold" hypernucleus from its ground or a low lying state. In this case, both the detected fragments have the same decay time with respect to the production time of hypernucleus.

In contrast, the two-step process results from a decay of two consecutive fissions or breakups with the two detected fragments come from different steps. This refers to the previously discussed first step strong fission decay of a "hot" hypernucleus with the none-strange fragment detected while a hyper-fragment produced and followed by second fission or break-up induced by the weak non-mesonic decay of the hyper-fragment. For the two-step process asso-

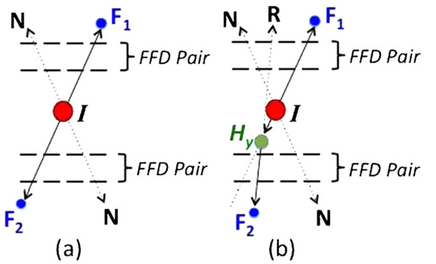

Fig. 7. Illustration of the two different processes that emit two fragments (labeled as F_1 and F_2) in coincidence, (a) one-step process (binary fission) and (b) two-step process (binary fission with formation of a hyper-fragment (H_y) followed by weak decay of hyper-fragment that emits a nucleus F_2 and recoil fragment R). The non-mesonic weak decay that causes the second step fission also emits a nucleon pair which is not shown in the illustration.

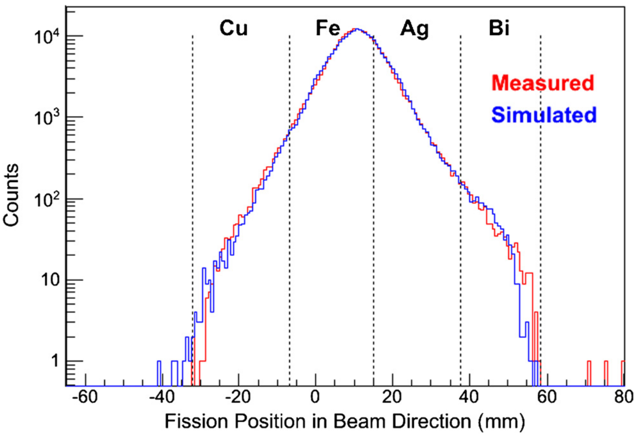

Fig. 8. Reconstructed fission position (in red) on the target foil, projected onto the beam direction (X). The target regions that are useful for lifetime measurements are marked. The beam centroid shift of 1.5 mm made a shift in the X direction of $\sim$10.7 mm, enhancing the statistics from the Ag and Bi targets. The distribution in blue is randomly selected events from the fitted beam profile function.

ciated with hyper-fragment production, the fragment from the first step has the "prompt" time, while the detected fragment from the second step has a delayed time from decay with respect to the "prompt" fragment. When two fragments are from different decay steps, their emission angles can be significantly away from back-to-back. Of course, strictly speaking, even the fragments from one-step fission will not have perfect back-to-back angle correlation since fission is always accompanied by emission of multiple nucleons. Therefore, the opening angle cannot be used effectively to separate the two types of processes. The time for the first step is so short so that it basically takes place inside of target. If both "cold" hypernuclei and hyper-fragments are able to escape the target, there is essentially no way to distinguish them.

4.3. Reconstructed fission position

To separate the events from different target materials, the fission position was reconstructed by using the intersection between the tilted target foil and the measured trajectory of the fragments. For each event, a fission position is given by each of the two independently measured fragments.

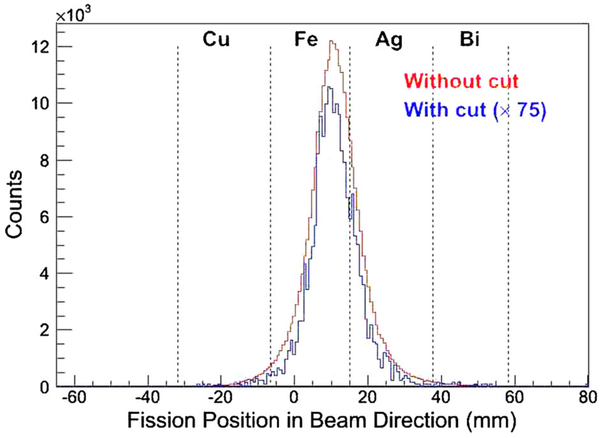

Fig. 9. Comparison of the measured fission position distributions with and without the L and R sum gate (±0.2 mm).

The event position on the foil was taken as the average of the two, as shown in red color in Fig. 8. The vertical dotted lines in the figure indicate the separation boundaries of the target materials. For the purpose of obtaining the beam intensity profile later, the fission position was projected along the beam direction (X). Due to insufficient position resolution, no separation gaps could be seen.

Since there was no U material successfully deposited onto the foil, no events were expected to appear in the region to the right of Bi. The edge of the Bi thus provided one reference of target material location. On the other side, the distribution was cutoff at the Au material predominantly by the FFD acceptance. This was verified by the simulation using Monte Carlo generated events with the fitted beam intensity profile (see later discussion). This provided the second reference of the target material location.

In addition, by applying a tight gate on the L and R sum (as discussed previously), events with significantly reduced position uncertainty can be selected, although the statistics reduction is dramatic. Fig. 9 shows the measured fission position on a linear scale. The histogram in blue was obtained by applying a gate, ±0.2 mm, to the L and R sums for each position plane. It was then scaled up by a factor of 75 to be shown on the same plot together with the un-gated distribution. A “dip” can be seen at the boundary between the Fe and Ag target regions, as expected.

4.4. Beam intensity profile and fission probability

The photon beam was generated by bremsstrahlung radiation from electrons incident on the thin target used by the HKS experiment, located ∼15 m upstream from the FFD system for this experiment. There was no active measurement of the photon intensity distribution. The intensity was highly peaked along the beam axis. The Cu and Bi targets were located away from the beam centroid so were radiated by the tail of the photon intensity distribution. The distribution of the reconstructed fission position reflects a combination of the beam intensity distribution and variation of production cross section and fission probability. As the beam was not centered in the beam pipe, photons at the tail of the distribution were lost when hitting the top portion of the beam pipe, enhancing the asymmetry at the target.

Table 2
The event mixing fractions in the target region selection. For example, of the total number of events selected from the Fe region gated by the fission position distribution (see Fig. 8), 0.6% and 2.9% of the events come from the Cu and Ag targets, respectively.

		Target region			
		Cu	Fe	Ag	Bi
Mixing Region	Cu	72.9%	0.6%	0%	0%
	Fe	27.1%	96.5%	34.8%	0%
	Ag	0%	2.9%	65.1%	28.0%
	Bi	0%	0%	0.1%	72.0%

By applying the position resolutions (as illustrated in Fig. 4) in the fragment detection, the emission angle correlation (see Fig. 6) between the two fragments, the FFD geometry, and locations of target regions, the combined (beam and fission) intensity function, a function of radius in the $Y - Z$ plane (see definition in Fig. 3), was obtained by fitting. This function contains two Gaussian functions with the same mean but different σ widths for an extended tail and a third Gaussian function with a shifted mean to account for the beam asymmetry. Using this fitted function, the simulated events reproduced the fission position distribution well, as seen in blue color in Fig. 8. The event mixing estimation was then done by the simulated events.

4.5. Mixing rate of events from different targets

Due to the position resolution, event mixing from different target regions could not be avoided. The mixing rate was estimated using the simulated events that were generated from separated target regions. The geometry of the FFD and targets, resolutions and all the characteristics discussed above were included in the simulation. The resulting estimated mixing rates are listed in Table 2. Such mixing must be taken into account when extracting the lifetime from decay time spectra. The mixing in the Fe target region is insignificant, while the other three target regions have significant event mixing from the neighboring target regions.

5. Decay time spectra and lifetime

5.1. Reconstruction of time zero and decay time

Time zero is the time when the fission takes place and the fragment is emitted. As discussed previously, this experiment did not have a external signal that could be used as the reference of the production time. The reference time was thus chosen to be the time signal from LPMWPC unit #1, the outer unit of the bottom TOF pair (see Fig. 3). Without a production time as the reference, the fission time zero could not be reconstructed by any single-fragment measurement from a TOF pair. It must be obtained by the relative information measured from the pair of fragments.

Using the measured TOF (i.e. $T_{12} = T_1 - T_2$ or $T_{43} = T_4 - T_3$) and the path length from positions measured by a pair of FFD units (#2/#1 or #3/#4), the full TOF (T_{01} or T_{04}) from the reconstructed fission position to the measured position at the outer unit #1 or #4 (see geometry in Fig. 3), can be determined by assuming a straight line path. The emission times from the target are thus $T_1 - T_{01}$ and $T_4 - T_{04}$. The time zero T_0 is defined as the relative difference of these two emission times as:

$$T_0 = (T_1 - T_{01}) - (T_4 - T_{04}). \tag{2}$$

T_0 should be zero if the two fragments come from a one-step fission process (prompt or delayed from weak decay). However, if the two fragments come from a two-step process, i.e. one from prompt fission in the primary step and the other one from delayed weak decay of a hyper-fragment, there will be a delay time appearing as a time shift. This time shift (i.e. delay time) can only be seen after canceling or removing the main part of TOF that depends on velocity in the T_0 calculation. Thus, the decay time spectrum can be obtained through a T_0 defined as the relative emission times of the two detected fragments.

There are three factors that predominantly affect the resolution of T_0. Under low pressure, the signal of an LPMWPC comes mainly from gas ionizations near the sense wires due to the Coulomb force from fragments with high Z. Large ranges of Z and mass A cause a large variation in signal sizes that influences the precision of time measurement by each individual LPMWPC unit. This factor varies depending on operational conditions related to beam, target and FFD geometry, as well as the Z and mass ranges of fragments. With relative time measurements, the velocity dependence makes it impossible to directly examine and correct the signal size dependence for individual events. Secondly, energy losses of the fragments in the low-pressure gas make a deviation from constant velocity which affects the calculation of TOF. Finally, the limited position resolution introduces errors in the determination of the geometric path length ratio of the two fragments and affects the calculated T_0 because of the tilted target geometry and wide opening angle range.

Fortunately, these influences appeared as clear correlations in the 2D plots of T_0 vs. T_{12}, T_{43}, $(T_4 - T_1)$, and ratio of the two path lengths, respectively. This provided an easy time correction to T_0. A linear fit was done to extract the correlation function for each correlation and T_0 was corrected by one correlation function at time. Iteration was needed until no correlation could be found to any of the above observables. The finalized T_0 spectrum is then characterized by the statistical distribution of decay time, i.e. a decay time spectrum which is independent of all the measured parameters.

5.2. *Characteristics of the decay time spectrum*

5.2.1. *Prompt and delayed components*

As T_0 is obtained from the relative emission times between the two fragments, the decay time spectrum should be therefore characterized by two dominant components. All events with coincident fragments from a one-step process should appear to be "prompt", including those from hypernuclear weak decay in one step from the primarily produced "cold" hypernuclei. Thus if a lifetime does exist in this T_0 spectrum, then it would not come from the "cold" hypernuclei.

The second component arises from the case in which a "hot" hypernucleus breaks up or fissions into a non-strange fragment and a hyper-fragment. In the two-step decay process, the hyper-fragment subsequently decays via weak-decay, emitting another nucleus. Thus the emission time of the prompt non-strange fragment becomes the reference time to that of the delayed fragment due to lifetime of hyper-fragment. Because the detectors do not distinguish between nuclei from the initial fission and hyper-fragment decay, the reference in T_0 can be reversed in time sequence and thus the T_0 distribution will be symmetric in two directions about the zero. Fig. 10 illustrates the final T_0 time spectrum obtained by the events selected from the Fe region.

The time spectrum obtained as described above receives contributions from hyper-fragments with wide mass and Z/A ratio ranges. They are lighter than the primarily photo-produced hypernuclei, i.e. "cold" hypernuclei. The lifetime extracted from this decay time spectrum should

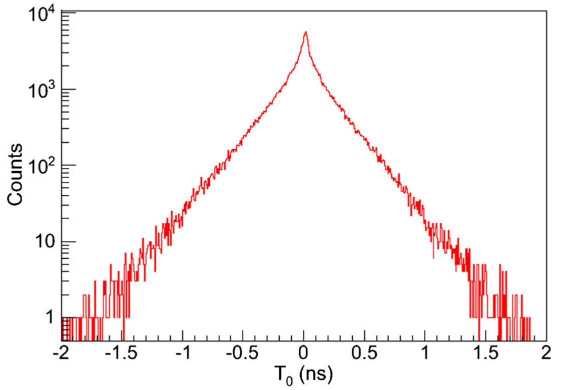

Fig. 10. The time spectrum obtained by the events selected from the Fe target region. $T_0 = 0$ is the absolute time zero and the decay time appeared in the $T_0 < 0$ region is due to reversed time reference between the two detected fragments.

therefore be a statistical average for a range of lighter hypernuclei. The range and statistical distribution are, unfortunately, not well known and could not be determined by this experiment.

5.2.2. In-flight and stopped decay of hyper-fragments

While all the observed T_0 spectra (as for an example that from Fe target shown in Fig. 10) do show exponential shapes (characteristic of a lifetime), the mechanism by which a hypernuclear lifetime would translate into an observed exponential in the spectrum is not trivial and must be verified. Both the hyper-fragment, H_y (as labeled in Fig. 7b) produced from the first step fission, and its decay product, F_2 produced from the second step fission due to hyper-fragment weak decay, can be in principle from decays in flight. The motion of H_y thus introduces a velocity dependent change in the apparent lifetime, distorting the exponential decay shape for the decay time spectrum. In the extreme, when the velocities of H_y and its weak decay fragment, F_2, are the same, there would be no time delay observed, i.e. the time delay due to lifetime of H_y would not be observed. In this case the time represents only the evolution time of the first step fission but not the lifetime of hypernuclei. Thus this is indistinguishable from a one step process. In contrast, if the hyper-fragment H_y stops in the target before decaying, then there would be no such influence, i.e. the lifetime should be characterized by an exponential distribution in the decay time spectrum. The time delay would come from lifetime of H_y, considering the evolution time for the first step is negligibly short in comparison to the lifetime of H_y. In other words, the question is whether the thin target and its arrangement does introduce energy loss that could have stopped significant amount of H_y for the exponential decay character to appear in the decay time spectrum.

The characteristics of the time spectra from in-flight and stopped decays can be investigated by a simple simulation model. Note here that the question to be answered is not affected by the different decay channels that emit F_2. The fragment F_2, can also be stopped, but this will not affect the spectrum shape as no coincidence event will be recorded in that case.

Since the properties of beam induced bismuth fission are well known [31], the simulation was modeled by considering the photo-production of the hypernucleus ${}^{209}_{\Lambda}$Pb (Λ plus a ^{208}Pb core) in the primary production step. In the model hypernuclei were created in an excited state with a mean mass 70 MeV above the two-body Λ threshold (i.e. 70 MeV above $B_\Lambda = 0.0$). A Gaussian distribution with a $\sigma = 40$ MeV about this mean was chosen to give a simplified mass distribution which was sufficient to generate a wide range of initial masses in the quasi-free region. For the purpose of this simulation, no specific hypernuclear states or resonances were necessary. The simulation assumed an average photon beam energy of $\sim$1.5 GeV, giving the primary hypernucleus a momentum of 300 MeV/c along the beam direction.

Referring to Fig. 7(b), the known features of Bi fission as induced by pion beams were employed for the first decay step of the primary hypernucleus. The fission was assumed to create a lighter hypernucleus H_y with a mass M_1, a lighter non-strange nucleus F_1 with a mass M_2, and a collection of eight neutrons which is an average number and was assumed for simplicity. The mean nucleon number for both M_1 and M_2 is $A_{MEAN} = 100$. A Gaussian spread with $\sigma_A = 30$ was applied to randomly generate ΔA and added to A_{MEAN} with opposite signs for M_1 and M_2. An average mass excess of -85 MeV/c^2 was applied when using [931.502 MeV/$c^2 \times (A_{\mathrm{MEAN}} + \Delta A)$] to determine M_2. In case of the hyper-fragment H_y, M_1 was generated in the same way but complimentary to M_2 with $-\Delta A$ and with the Λ mass included. In both cases, a fixed average Z/A ratio was assumed for the proton number Z. In addition, the hyper-fragment H_y was assumed to be in its ground state. Thus an additional -15 MeV binding energy was simply included in its mass. Finally, the vector momenta of both F_1 and H_y for each fission event were calculated using ten-body phase space.

In the second step, H_y was assumed simply to decay by one of the non-mesonic modes as $H_y \to F_2 + 2n$, i.e. into a non-strange nuclear fragment F_2 in the ground state plus two neutrons with a 3-body phase space. Other decay modes only change slightly the mass and charge of F_2 and thus its energy loss. Whether H_y could be stopped is what needs to be verified by the simulation. Therefore, the mass of F_2 in the simulation was simply determined in the same way as that of F_1. No change in Z was assumed. The time of decay of H_y was chosen randomly with an assumed lifetime of 200 ps. The non-strange fragment F_1 was assumed not to decay before being detected.

From the masses and resultant momenta of F_1 and F_2, the detected positions and times at each LPMWPC unit were calculated. The simulated fission events were filtered by the size of LPMWPC units (acceptance) and the coincidence requirement that F_1 and F_2 be detected by the TOF arms in opposite directions. The same time zero reconstruction was then done for both F_1 and F_2 from their TOF's and trajectory geometries. T_0 was obtained using one of the two arms as a fixed time reference as discussed in the previous sections for the real measurement. Finally, T_0 was spread by a 50 ps resolution.

Fig. 11 shows the T_0 spectrum of simulated events that come from two-step processes without taking into account the energy loss in the target. In this case, all hyper-fragments (H_y) decay in-flight. Since the target is very thin, the time spent traveling through the target is negligibly small in comparison to the lifetime. The symmetry for $T_0 < 0$ and $T_0 > 0$ regions is expected, and the spectrum shows an obviously extended tail from time delay due to lifetime of the hyper-fragments H_y. However, the spectrum is severely distorted from a pure exponential shape by the variation in the location of H_y when it decays, as it depends on its velocity and direction of flight. In comparison, if all the hyper-fragments H_y are forced to be at rest from the moment of its creation, the time distribution (in red) is purely exponential and matches the lifetime assumed in the simulation. Given the exponential feature in the experimentally obtained T_0 spectrum, shown in Fig. 10, energy loss must have played a crucial role and stopped a significant fraction of hyper-fragments.

Since many important parameters in the first step are unknown, such as the precise photon energy distribution, the actual mass distribution of the excited hypernuclei and their momenta, and the variations of mass and ratio of Z/A of the hyper-fragments as well as their non-strange

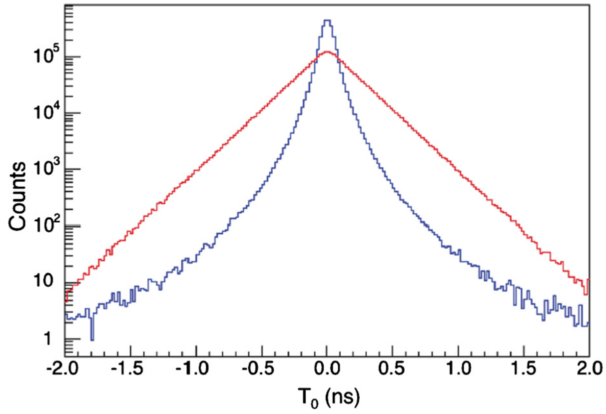

Fig. 11. The time spectrum (blue) obtained by simulated hyper-fragment decay from a two-step process without taking into account energy loss in the target. The red spectrum is the same two-step process, but with the hyper-fragment H_y forced to decay at rest.

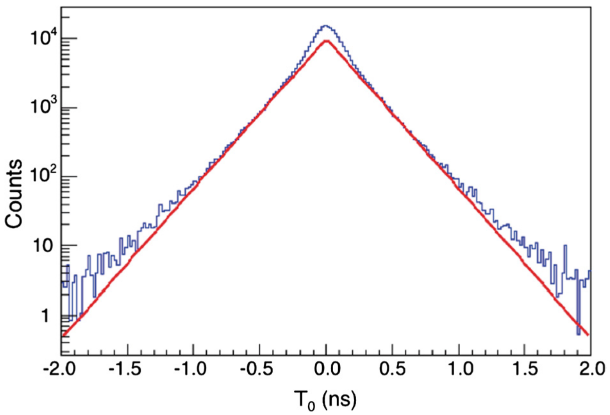

Fig. 12. The time spectrum (blue) obtained by simulated hyper-fragment decay from a two-step process, taking into account energy loss in the target. The red lines are exponentials with a time constant of 200 ps, the hyper-fragment lifetime used in the simulation.

partners from fission, a precise simulation is not possible. Therefore, the same simplified simulation mentioned above was used to test the effect of energy loss on H_y, as well as F_1 and F_2 although their energy loss may only affect the event yield. To simplify the application of energy loss of ions, a simple analytic energy loss for ions in form of $dE/dx = -Cx^{1/2}$ was applied to calculate range or final energy after passing through a given target thickness. Only ionization loss was considered. The simulation was not aimed to precisely reproduce the decay time spectrum but to study the character of decay time spectrum with the effect of energy loss.

Fig. 12 shows the T_0 spectrum using simulated events from the Bi target with the above simplified generic energy loss included. An exponential region with a slope that agrees with the lifetime used in the simulation appears and the energy loss becomes sufficient for a significant amount of hyper-fragments to stop in the target before decaying. The range of this linear region depends on the ratio of the number of stopped decays over that of in-flight decays. Good linearity appears to begin at $|T_0| = \sim 0.3$ ns when the in-flight decay events contribute less than a few % at any decay time. At the time (an upper time limit) when the in-flight decay events become statistically significant, the feature of in-flight decay tail starts to be visible. However, the total number of events beyond this upper limit may not be statistically significant to influence a lifetime fit. Therefore, it can be concluded that energy loss played key role in the experimentally obtained T_0 spectra and the ability to fit a lifetime from the decay time spectra. The in-flight decay makes crucial influence only in the region of $|T_0| < \sim 0.3$ ns. Although the simulation is rather generic and far from realistic, it is sufficient for verification of the features seen in the experimentally obtained T_0 spectra.

Simulations were also done by giving large Z/A ratio variations and the above conclusion remained unchanged, except the number of events with both F_1 and F_2 being detected varied. In addition, using zero lifetime the prompt decay was also studied by comparing the ratios of number of events of prompt over delayed fission of hyper-fragments from the Fe and Bi targets. The energy loss from the Bi target appeared causing five time more event loss of prompt decay than that from the Fe targets. This may simply come from higher energy loss in the higher Z target that causing event loss of prompt decay while a larger release energy from non-mesonic decay gives a better chance for F_2 to escape from target.

As an example, the T_0 spectrum (Fig. 10) obtained from the Fe target shows a significantly longer linear region than that from the simulation with energy loss. The starting point of this linear region appears to be in good agreement at $|T_0| = \sim 0.3$ ns, while the mixed in-flight decay tail enhancement is not quite tangible.

6. Fitting for lifetime from the T_0 spectrum

6.1. *Fitting method and functions*

For the events selected from the Fe target region, the limited position resolution only mixes in about 0.6% and 2.9% from the neighboring Cu and Ag regions, as shown in Table 2. The influence of this contamination on lifetime fitting is negligible and thus the decay time spectrum of the events selected in the Fe region can be assumed to contain only one lifetime. Therefore the Fe spectrum (Fig. 10) can be described by three components: 1) A prompt distribution, 2) An in-flight decay time distribution and 3) A decay time distribution.

Prompt distribution – This component is in the region of $|T_0| < \sim 0.3$ ns and formed by the events primarily from prompt fission with zero lifetime and the one-step process of hypernuclear weak decay with the two fragments having the same reference time, as described previously. This distribution can be described by a Gaussian function and its width should represent the time resolution.

In-flight decay distribution – As discussed above, the contribution of this component is also mainly in the same region as the prompt component. The shape of the distribution depends on multiple factors related to variations of the velocity vector difference, angular distribution, and energy loss associated with the target geometry. Due to such complications it is impossible to formulate a precise analytic function. However, since the statistics from the tail of this component in the linear region where a lifetime is to be fitted is small and mainly affects the statistical uncertainty, its distribution can also be approximated by a Gaussian function. In other words, the long tail of the in-flight decay distribution with relatively low statistics can be ignored in the linear region. The assumed Gaussian function is only to provide a reasonably good description of the time spectrum in the central region, i.e. $|T_0| < \sim 0.3$ ns.

Beyond the linear region, the in-flight decay tail becomes increasingly dominant. Thus, the lifetime fitting must have an upper limit. Combining these two components, the overall in-flight distribution was then described by two Gaussians as:

$$R(t) = A[e^{-(t-t_{01})^2/(2\sigma_1^2)} + Ke^{-(t-t_{02})^2/(2\sigma_2^2)}] \tag{3}$$

$$= A[R_1(t) + KR_2(t)], \tag{4}$$

where t_{01} and t_{02} are the means of the prompt and in-flight decay distributions. They are both expected to be very close to $T_0 = 0$ and may be slightly different from each other due to the imperfect description of the in-flight decay distributions as a Gaussian. σ_1 and σ_2 are the widths of the two Gaussians. Because of the approximation, the time resolution cannot be represented solely by either σ_1 or σ_2.

The resolution was later determined based on the best fit (i.e. minimized χ^2) for the lifetime from the linear region. This time resolution is expected to be consistent in the spectra from all targets. K is the ratio between the two Gaussians while A is the normalization such that,

$$\int_{-\infty}^{\infty} R(t)dt = 1. \tag{5}$$

The normalization is necessary in order to obtain the total number of events in the fitted distribution. However, due to approximation of in-flight decay, the ratio K may not precisely represent the ratio between prompt and in-flight decay events.

Decay time distributions – The decay time distributions (i.e. the linear region) appear and dominate in the region of $|T_0| > \sim 0.3$ ns and an upper time limit which varies among the four targets depending on statistics. The total delayed decay events were randomly distributed in two regions, $T_0 > 0$ and $T_0 < 0$, due to the order of time reference between the two fragments. They formed two independent decay time spectra. The corresponding decay probability functions are:

$$P_+(t) = B_+ \int_{-\infty}^{\infty} R_s(t-t')e^{-\frac{t}{\tau_+}}dt'(t > 0),$$

$$P_-(t) = B_- \int_{-\infty}^{\infty} R_s(t-t')e^{\frac{t}{\tau_-}}dt'(t < 0) \text{ and} \tag{6}$$

$$\int_{-\infty}^{\infty} P_\pm(t)dt = 1.$$

$B_\pm$ are the normalization constants, $R(t-t')$ is the response function corresponding to the time resolution of T_0 reconstruction, and $\tau_\pm$ are the two lifetimes to be independently fit from the $T_0 > 0$ and $T_0 < 0$ regions.

The full range time spectrum is thus, in principle, described by the combined function:

$$T(t) = N_p R(t) + N_{d+} P_+(t) + N_{d-} P_-(t), \tag{7}$$

where N_p, N_{d+}, and N_{d-}, are the numbers of events in the corresponding components. However, since each of the two decay distributions, $P_+(t)$ and $P_-(t)$ with convolution of the time response function, actually extend into the opposite region, it is not technically easy (if not impossible) to carry out a full range fit using such a combined function expressed by Eq. (7). To solve this problem, the spectrum was separately fitted by two partial functions:

$$\begin{aligned} &T_+(t) = N_{p+}R(t) + N_{d+}P_+(t)(t > 0) \text{ and} \\ &T_-(t) = N_{p-}R(t) + N_{d-}P_-(t)(t < 0). \end{aligned} \tag{8}$$

Due to the limitation of T_0 reconstruction correction, the spectra from the two sides were not expected to be perfectly symmetric. Thus, there will be deviations between the parameters of the same kind fitted from the two time regions. However, these deviations are minimized when the lifetime τ is taken to be the statistical average of τ_+ and τ_-.

The response function R_s in Eq. (6) takes the same form as the time resolution that, however, could not be directly obtained in this experiment. It was assumed that it remains fixed for spectra from all targets and for both $T_0 > 0$ and $T_0 < 0$ regions. The sensitivity of its form was investigated by assuming (1) a simplified single Gaussian function with a σ width and (2) the identical form described by Eq. (3). It was found that an optimized χ^2 per number of degrees of freedom (NDF) could be reached by giving the single Gaussian width in a wide range of σ from 35 to 60 ps while the fitted $\tau_\pm$ varied very little, significantly less than the statistical uncertainty. In addition, the sensitivity to the form of the response function was found to be negligible. By investigating the consistency in optimized fitting of all spectra, the time resolution was estimated to be $\sigma{\sim}38$ ps and consistent in fitting all the T_0 spectra for both $T_0 > 0$ and $T_0 < 0$ regions using a single Gaussian function for simplicity.

6.2. *Fitting the T_0 spectrum from the Fe target*

6.2.1. *The Fe time spectrum in the $T_0 > 0$ region*

The $T_0 > 0$ part of the Fe time spectrum was fitted by the function $T_+(t)$ defined in Eq. (8). The upper fitting limit (i.e. the boundary of the upper linear region) was chosen to be at $T_0 = 1.2$ ns.

There are total of nine (9) parameters from the two Gaussian functions and the convoluted decay function. These parameters, P_i with $i = 1$ to 9, are N_{p+}, K_+, t_{01+}, σ_{1+}, t_{02+}, σ_{2+}, N_{d+}, τ_+, and t_{0d+}, forming a correlation matrix. The parameters $P_{3,5,9}$, (i.e. t_{01+}, t_{02+}, and t_{0d+}) are the time shifts added to the two Gaussians and the decay functions to take into account imperfect time corrections and bin-effects. The others are defined in Eq. (3), Eq. (6), and Eq. (8), for the $T_0 > 0$ region. In carrying out the multi-parameter fitting, the corresponding covariance matrix Σ is then a 9×9 matrix, where the diagonal terms are σ_i^2 (the square of statistical uncertainty of P_i) and the off diagonal terms are $\rho_{ij}\sigma_i\sigma_j$ with $i, j = 1$ to 9. ρ_{ij} are the correlation coefficients.

The confidence region for this multivariate fit parameter set is defined by, $\chi^2 \le \chi^2_{min} + \Delta\chi^2$, where χ^2_{min} is the χ^2 found when fitting the data and $\Delta\chi^2$ defines the confidence region [32]. To set a 90% probability content for this nine-parameter multivariate fit, $\Delta\chi^2$ was then chosen to be 14.68 (see Table 7.1 on Page 46 of the MINUIT reference manual [33]). Using this confidence region, the values (P_i) and statistical uncertainties (σ_i) of the parameters in the correlation matrix yielded by the fitting are listed in Table 3. The lifetime τ_+ fit from the $T_0 > 0$ region was found to be 208.9 ± 4.9 (stat.) ps. The χ^2/NDF $= 1.18$ with NDF $= 259$. Table 4 shows the correlation coefficients, ρ_{ij}. The values of the corresponding covariance matrix can be calculated by the definitions given above. The correlations between these parameters signify their statistical uncertainties within the defined CL $= 90\%$ confidence region. However, the lifetime τ_+ does not have significant correlations to most of the other parameters. In other words, the influence from

Table 3
The values (P_i) and statistical uncertainties ($\pm\sigma_i$) obtained by the multivariate fitting for the $T_0 > 0$ region of the Fe time spectrum.

$P_1(N_{p+})$ $\pm\sigma_1$	$P_2(K_+)$ $\pm\sigma_2$	$P_3(t_{01+})$ $\pm\sigma_3$	$P_4(\sigma_{1+})$ $\pm\sigma_4$	$P_5(t_{02+})$ $\pm\sigma_5$	$P_6(\sigma_{2+})$ $\pm\sigma_6$	$P_7(N_{d+})$ $\pm\sigma_7$	$P_8(\tau_+)$ $\pm\sigma_8$	$P_9(t_{0d+})$ $\pm\sigma_9$
3882.7	0.440	−0.026	0.075	0.0188	0.0145	569.3	0.2089	0.027
595.2	0.090	0.025	0.014	0.0015	0.0021	59.5	0.0049	0.022

Table 4
The corresponding correlation coefficients, ρ_{ij}, obtained from the multivariate fitting for the $T_0 > 0$ region of the Fe time spectrum.

ρ_{ij}	Global	P_1	P_2	P_3	P_4	P_5	P_6	P_7	P_8	P_9
P_1	0.9862	1.000	0.779	−0.688	0.082	−0.481	0.051	−0.927	−0.047	−0.932
P_2	0.9791	0.779	1.000	−0.366	−0.311	−0.440	−0.083	−0.860	−0.177	−0.922
P_3	0.9873	−0.688	−0.366	1.000	−0.691	0.336	−0.610	0.652	−0.043	0.607
P_4	0.9811	0.082	−0.311	−0.691	1.000	−0.055	0.679	−0.095	0.398	0.083
P_5	0.5805	−0.481	−0.440	0.336	−0.055	1.000	−0.116	0.525	0.017	0.520
P_6	0.8881	0.051	−0.083	−0.610	0.679	−0.116	1.000	−0.169	0.192	−0.081
P_7	0.9894	−0.927	−0.860	0.652	−0.095	0.525	−0.169	1.000	−0.064	0.947
P_8	0.7860	−0.047	−0.177	−0.043	0.398	0.017	0.192	−0.064	1.000	0.179
P_9	0.9939	−0.932	−0.922	0.607	0.083	0.520	−0.081	0.947	0.179	1.000

Table 5
The values (P_i) and statistical uncertainties ($\pm\sigma_i$) obtained independently by the multivariate fitting for the $T_0 < 0$ region of Fe time spectrum.

$P_1(N_{p-})$ $\pm\sigma_1$	$P_2(K_-)$ $\pm\sigma_2$	$P_3(t_{01-})$ $\pm\sigma_3$	$P_4(\sigma_{1-})$ $\pm\sigma_4$	$P_5(t_{02-})$ $\pm\sigma_5$	$P_6(\sigma_{2-})$ $\pm\sigma_6$	$P_7(N_{d-})$ $\pm\sigma_7$	$P_8(\tau_-)$ $\pm\sigma_8$	$P_9(t_{0d-})$ $\pm\sigma_9$
3924.1	0.443	0.066	0.079	0.0178	0.0150	385.4	0.2157	0.049
415.3	0.0596	0.018	0.017	0.0015	0.0021	32.6	0.0050	0.015

the prompt and in-flight decay components are rather confined in the region of $T_0 < 0.3$ ns, at least for the Fe case in which the events from decay at rest have sufficient statistics.

6.2.2. The Fe time spectrum in the $T_0 < 0$ region

A multivariate fit was carried out independently for the $T_0 < 0$ region in the same way as that for the $T_0 > 0$ region. The function is defined in Eq. (8) as $T_-(t)$ with nine parameters in the same definition as those for $T_+(t)$. The same response function was used, i.e. assuming the time resolution is constant in all measurements. The upper fitting limit was then chosen to be −1.2 ns. The T_0 spectrum was not assumed to be perfectly symmetric due to uncertainties in time corrections. Thus, the fitting was independent of the fitting done for the $T_0 > 0$ region. The fitted values (P_i) and statistical uncertainties (σ_i) of the parameters in the X matrix and the corresponding correlation coefficients in the covariance matrix Σ are shown in Table 5 and Table 6, respectively.

The fitting for the $T_0 < 0$ region yielded similar results to the $T_0 > 0$ region. The values of all the fitted parameters agreed with the corresponding ones from the positive region within one σ uncertainty. The obtained lifetime τ_- fitted from the $T_0 < 0$ region was found to be 215.7 ± 5.0 (stat.) ps. The $\chi^2/\mathrm{NDF} = 1.13$ with $\mathrm{NDF} = 255$.

Table 6
The corresponding correlation coefficients, ρ_{ij}, obtained from the multivariate fitting for the $T_0 < 0$ region of Fe time spectrum.

ρ_{ij}	Global	P_1	P_2	P_3	P_4	P_5	P_6	P_7	P_8	P_9
P_1	0.9748	1.000	0.582	−0.144	−0.454	0.463	−0.093	0.812	−0.149	0.883
P_2	0.9637	0.582	1.000	−0.601	−0.800	0.384	−0.212	0.826	−0.282	0.839
P_3	0.9747	−0.144	−0.601	1.000	0.853	−0.146	0.678	−0.353	0.189	−0.308
P_4	0.9851	−0.454	−0.800	0.853	1.000	−0.258	0.521	−0.724	0.473	−0.640
P_5	0.5686	0.463	0.384	−0.146	−0.258	1.000	−0.004	0.472	−0.095	0.517
P_6	0.8823	−0.093	−0.212	0.678	0.521	−0.004	1.000	−0.075	0.176	−0.008
P_7	0.9855	0.812	0.826	−0.353	−0.724	0.472	−0.075	1.000	−0.419	0.957
P_8	0.8005	−0.149	−0.282	0.189	0.473	−0.095	0.176	−0.419	1.000	−0.294
P_9	0.9943	0.883	0.839	−0.308	−0.640	0.517	−0.008	0.957	−0.294	1.000

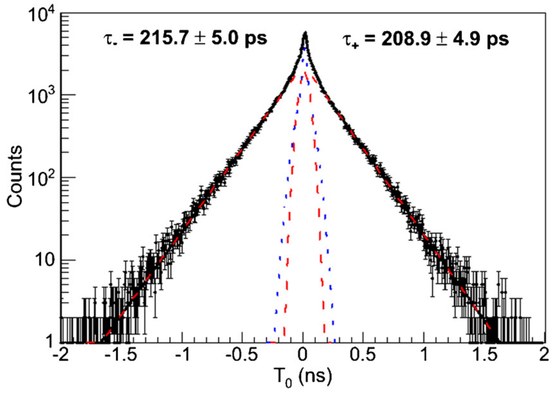

Fig. 13. The time spectrum from the Fe target with the fitted functions overlaid. The dashed line with blue color around the center is the combined Gaussian functions fitted from both sides, describing the prompt and in-flight decays. The two dashed lines with red color extending in opposite directions are the two convoluted decay functions measured independently in opposite time references between the two detected fragments.

Fig. 13 shows again the time spectrum obtained by the events selected from the Fe target region with the fitted functions defined by Eq. (8). The fitted Gaussian functions as defined by Eq. (3) for the prompt and in-flight decays are shown by a dashed line with blue color. The two fitted decay functions described by Eq. (6) are illustrated by two dashed lines with red color. The lifetime was then independently measured from the $T_0 < 0$ and $T_0 > 0$ regions. Taking the statistical average of τ_+ and τ_-, using their uncertainties to define the statistical weights, the lifetime τ(Fe) was then found to be 212.2 ± 3.5 ps. By using this average, the influence of imperfect time corrections is minimized.

6.2.3. Partial range fitting

Since the influence from the prompt and in-flight decays to the fitted lifetime is small, a fit can also be done within a partial range defined by $|T_0| > 0.3$ ns and $|T_0| < 1.2$ ns, using simply the decay function described by Eq. (6). In this case, only three parameters are involved. $\Delta\chi^2$ was then adjusted accordingly within the same 90% confidence region. Fig. 14 shows the result of such a partial range fit for the Fe time spectrum. The fitted decay functions convolved by the time resolution of 38 ps in the two regions are plotted as the red dashed lines.

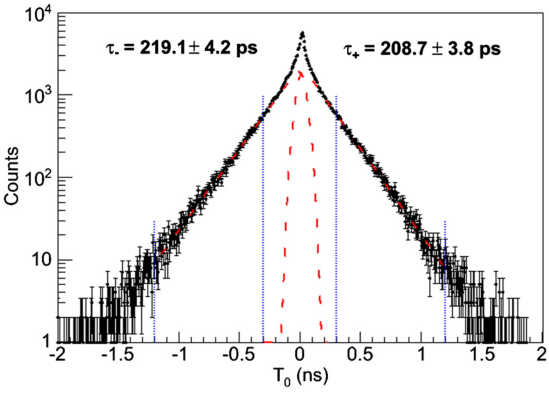

Fig. 14. The time spectrum from the Fe target with the fitted decay functions illustrated by the red dashed lines. The fit was made only in the linear region defined between $|T_0| > 0.3$ ns and $|T_0| < 1.2$ ns.

The fitted τ_+ and τ_- are 208.7 ± 3.8 ps ($\chi^2/\mathrm{NDF} = 1.07$ with NDF $= 133$) and 219.1 ± 4.2 ps ($\chi^2/\mathrm{NDF} = 0.95$ with NDF $= 133$), respectively. Taking the statistical average of these two, the lifetime τ(Fe) from partial range fit is 213.4 ± 2.8 ps. These results are consistent with those from the full range fit within a 1σ uncertainty. This simply shows that the lifetime predominantly depends on the linearity of the logarithm in the decay region of the time spectrum.

6.3. Fitting for double lifetime

Each of the time spectra built by the events selected from the Cu, Ag and Bi target regions have two decay components due to a significant mixing of events from one of the adjacent targets because of the limited position resolution. The number of such mis-placed events ranges from $\sim 27\%$ to $\sim 35\%$ (see Table 2) out of the total events selected from the chosen target regions. This means that each of these three time spectra must be considered to contain two decay components and thus two potentially different lifetimes.

Such a mixed spectrum can be viewed as a sum of one component with a known lifetime and another with unknown lifetime that will be fitted, given that the ratio of the two groups of events is known. In other words, the convolved decay function has to contain two components with known ratio between them with one of the two lifetimes is known and fixed. In the case of fitting the spectra from the Ag and Cu target regions, the known component is from Fe with a mixing rate of 34.8% and 27.1% of total, respectively. The previously obtained values of τ_+(Fe) and τ_-(Fe) from full range fitting were used as the known lifetime to fit for the lifetime τ(Ag) and τ(Cu). Subsequently, when fitting for τ(Bi), τ(Ag) was then treated as known with a mixing event rate of 28%.

Fitting for spectra containing double lifetimes was first tested by a Monte Carlo generated decay time spectrum mixed with events containing two different lifetimes, τ_1 and τ_2. τ_1 was the lifetime of the known component and was fixed at 200 ps. The number of events from the known component was chosen to be 34%. The lifetime $\tau_2^{\mathrm{Assumed}}$ was artificially given to be from 120 ps to 190 ps, incremented by 10 ps each time, to generate the unknown component. The statistics were based on the number of events selected from the Bi target region. No prompt and in-flight decays were considered in this test.

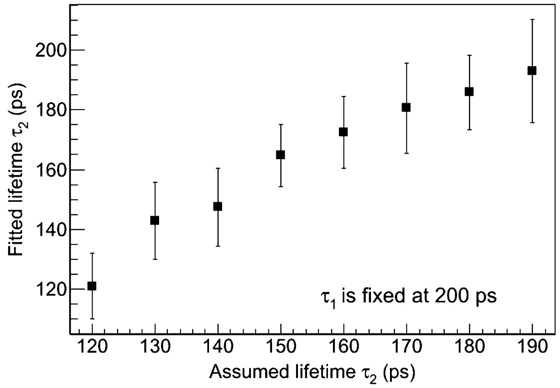

Fig. 15. Correlation between the fitted and the assumed τ_2 under the influence of the known component with τ_1 and a mixing ratio of 34%. The statistics were based on the number of events selected from the Bi target region.

The spectrum was then fitted for τ_2^{Fitted} which was compared to τ_2^{Assumed}. Fig. 15 shows the correlation of the fitted τ_2^{Fitted} versus the assumed τ_2^{Assumed}. The difference between τ_2^{Fitted} and τ_2^{Assumed} is less than 1σ of the statistical uncertainty. This test showed that the unknown lifetime can be obtained reasonably well in wide range of lifetimes by our fitting method with the known component contributing up to 34%.

6.3.1. Fitting the Ag time spectrum

By fixing the component associated with Fe, the known mixing ratio (34.8% as shown in Table 2) and the previously obtained lifetime $\tau_+(\text{Fe}) = 208.9$ ps and $\tau_-(\text{Fe}) = 215.7$ ps from the full range fit, the time spectrum of Ag was fit in the same way as done for the Fe time spectrum with 9 variables in each of the $T_0 > 0$ and $T_0 < 0$ regions. Since the Ag target was also near the center of the photon beam, the spectrum had high statistics so that the range of the linear region is similar to that in the Fe spectrum. Thus the upper limits were also chosen to be $|T_0| < 1.2$ ns to cut away the tail region where in-flight decay dominates. The time resolution was found to be $\sigma \sim 38$ ps, consistent with that of the Fe target. The lifetimes $\tau_+(\text{Ag})$ and $\tau_-(\text{Ag})$ were fit as 208.0 ± 7.3 ps (χ^2/NDF $= 0.96$ and NDF $= 250$) and 210.5 ± 5.8 ps (χ^2/NDF $= 0.96$ and NDF $= 234$), respectively. The level of correlations between the 9 variates in each region are similar to those seen in Tables 4 and 6 in the case of the Fe time spectrum fitting. Fig. 16 shows the time spectrum from the Ag target with the fitted functions overlaid. The dashed line with blue color around the center is of the combined Gaussian functions fitted from both sides, describing the prompt and in-flight decays. The two red dashed lines extending in opposite directions are the two convoluted decay functions (each has two components – one known and one fitted) measured independently in opposite time references between the two detected fragments. Taking the statistical average of τ_+ and τ_- and using their uncertainties to define the statistical weights, the lifetime $\tau(\text{Ag})$ is then found to be 209.5 ± 4.5 ps.

The simpler partial range double lifetime fit with only three variables was also done within a partial range defined by $|T_0| > 0.3$ ns and $|T_0| < 1.2$ ns to check the consistency. The fit τ_+ and τ_- are 206.3 ± 6.4 ps ($\chi^2/\text{NDF} = 0.77$ with NDF $= 133$) and 203.5 ± 5.8 ps ($\chi^2/\text{NDF} = 0.998$ with NDF $= 133$), respectively. Fig. 17 shows the result of the partial range fit. Taking the statistical average of these two, the lifetime $\tau(\text{Ag})$ from partial range fit is 204.8 ± 4.3 ps. The result is consistent to that from the full range fit within a 1σ uncertainty.

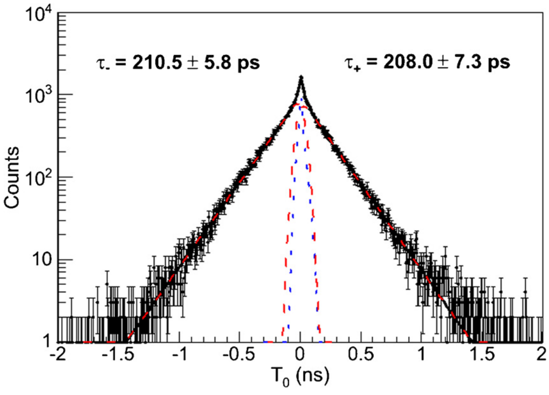

Fig. 16. The time spectrum from the Ag target with the fitted functions overlaid. The dashed line with blue color around the center is the combined Gaussian functions fitted from both sides, describing the prompt and in-flight decays. The two dashed lines with red color extending in opposite directions are the two convoluted decay functions (each has two components – one known and one fitted) measured independently in opposite time references between the two detected fragments.

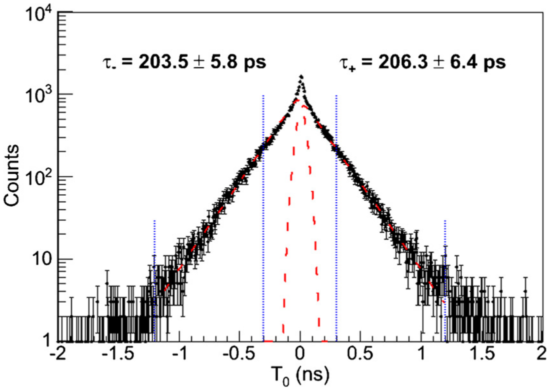

Fig. 17. The time spectrum from the Ag target with the fitted decay functions containing two components illustrated by the red dashed lines. The fit was done only to the linear region defined between $|T_0| > 0.3$ ns and $|T_0| < 1.2$ ns.

6.3.2. Fitting the Cu and Bi time spectra

Both the Cu and Bi targets were located away from the beam center and illuminated only by the tail of the bremsstrahlung photon beam. Therefore, these two time spectra had significantly lower statistics. In addition, the Bi target had a thinner thickness, making its statistics lower than that from the Cu target. Thus larger bin sizes were used for plotting the Cu and Bi time spectra.

For a decay time spectrum using log scale for number of events, the slope of the fitted straight line corresponds to the lifetime. Lower statistics has two effects on the fitting and statistical uncertainty. First of all, the range of the linear region in which the in-flight decay tail has minimum influence to the fitted result is reduced, meaning the upper fit limit has to be reduced to cut away the long tail region where the in-flight decay is dominant (Fig. 12). Secondly, the linearity within the defined linear region becomes poor and larger statistical uncertainty from a fitting is expected.

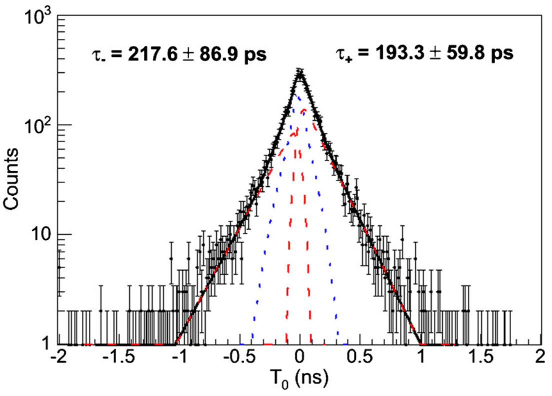

Fig. 18. The time spectrum from the Cu target with the fitted functions overlaid. The dashed line with blue color around the center is the combined Gaussian functions fitted from both sides, describing the prompt and in-flight decays. The two dashed lines with red color extending in opposite directions are the two convoluted decay functions (each has two components – one known and one fitted) measured independently in opposite time references between the two detected fragments.

Using multi-variate fit, the upper fitting limit for these two spectra was studied and chosen to be $|T_0| < 0.9$. This limit minimizes the statistical uncertainty on the lifetime. The time resolution was found to be consistent to that for the Fe and Ag spectra, i.e. $\sigma \sim 38$ ps.

Similar to the Ag time spectrum, each of the Cu and Bi spectra had one extra fixed decay component (see Table 2) as the Ag spectrum had. In case of Cu, 27.1% of events came from Fe, while for Bi 28% were from Ag. A double lifetime fit was applied in the same way as for fitting the Ag time spectrum.

In case of the Cu time spectrum, the full range of which was fit with 9 variables in each of the $T_0 > 0$ and $T_0 < 0$ regions, the lifetimes τ_+(Cu) and τ_-(Cu) were found to be 193.3 ± 59.8 ps (χ^2/NDF = 0.9 with NDF = 66) and 217.6 ± 86.9 ps (χ^2/NDF = 0.9 with NDF = 66), respectively. Comparing the error matrix to that from fitting of the Fe spectrum, increased correlations were found only with the parameters representing the fitted total number of prompt and delayed decay events. The large statistical uncertainty is mainly due to low statistics. The statistical average of the two (weighted by their statistical uncertainties) gives the lifetime τ(Cu) of 201.1 ± 49.3 ps. Fig. 18 shows the time spectrum from the Cu target with the fitted functions overlaid in the same way as that for the Ag spectrum.

Furthermore, the partial range fit (Fig. 19) between $|T_0| > 0.3$ ns and $|T_0| < 0.9$ ns for the two regions gave τ_+(Cu) = 203.9 ± 31.3 ps (χ^2/NDF = 0.94 with NDF = 57) and τ_-(Cu) = 206.3 ± 32.9 ps (χ^2/NDF = 0.97 with NDF = 57). The statistical average of the two is then 205.0 ± 22.7 ps.

Similar to the Cu case, the fit of the Bi time spectrum showed the same characteristics, except for the significantly larger statistical uncertainty due to low statistics. From the fitting of the 9 variables, the lifetimes τ_+(Bi) and τ_-(Bi) were found to be 233.7 ± 72.2 ps (χ^2/NDF = 0.93 with NDF = 21) and 211.8 ± 58.8 ps (χ^2/NDF = 1.18 with NDF = 21), respectively (Fig. 20). The statistical average is then 220.5 ± 45.6 ps. The partial range fit (Fig. 21), on the other hand, gave τ_+(Bi) = 234.8 ± 75.1 ps (χ^2/NDF = 0.73 with NDF = 13) and τ_-(Bi) = 193.0 ± 69.2 ps (χ^2/NDF = 1.17 with NDF = 13). The statistical average is 212.2 ± 50.9 ps.

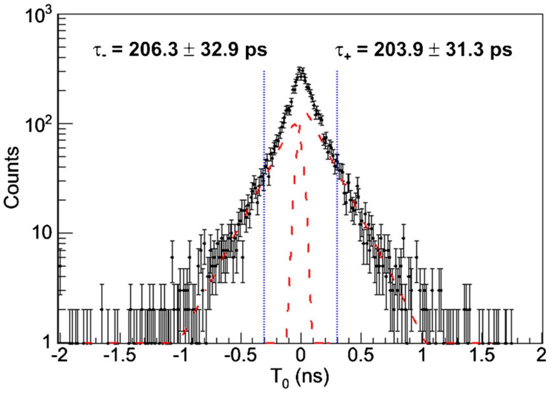

Fig. 19. The time spectrum from the Cu target with the fitted decay functions containing two components illustrated by the red dashed lines. The fit was done only to the linear region defined between $|T_0| > 0.3$ ns and $|T_0| < 0.9$ ns.

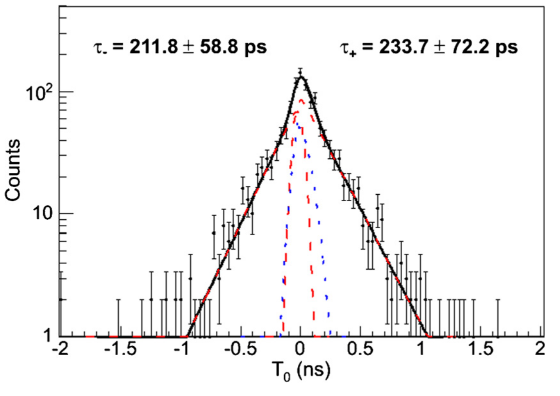

Fig. 20. The time spectrum from the Bi target with the fitted functions overlaid. The dashed line with blue color around the center is the combined Gaussian functions fitted from both sides, describing the prompt and in-flight decays. The two dashed lines with red color extending in opposite directions are the two convolved decay functions (each has two components – one known and one fitted) measured independently in opposite time references between the two detected fragments.

6.4. Systematic uncertainty

The systematic uncertainty is mainly from the methodical uncertainty of the fitting method. Using Monte Carlo generated events with a given lifetime, this systematic uncertainty was studied with various fitting limits as well as different $R(t)$ and $R(t - t')$ functions. This uncertainty was found to be on the level of $\sim \pm$ 10 ps.

7. Lifetime result and feature of the measurement

The lifetimes obtained by full range fit within the confidence region defined at 90% from the regions of $T_0 > 0$ and $T_0 < 0$ as well as their statistical average for the four different targets are summarized in Table 7. As discussed previously, these measured lifetimes do not represent

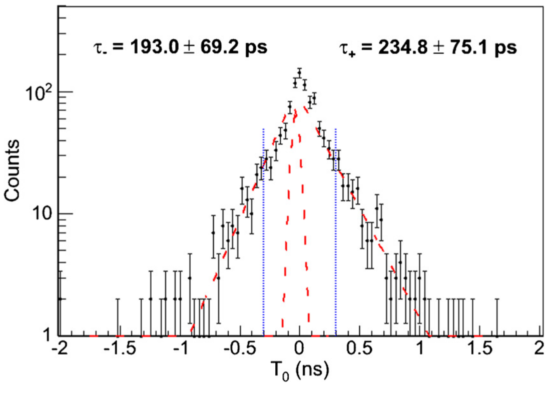

Fig. 21. The time spectrum from the Bi target with the fitted decay functions containing two components illustrated by the red dashed lines. The fit was done only to the linear region defined between $|T_0| > 0.3$ ns and $|T_0| < 0.9$ ns.

Table 7
Summary of the lifetimes measured (with full range fit) from time spectra obtained by the events selected from the four target regions. The uncertainty is statistical and systematic uncertainty is $\sim \pm$ 10 ps.

Target	$\tau_+ \pm \delta\tau$ (ps)	χ^2/NDF	NDF	$\tau_- \pm \delta\tau$ (ps)	χ^2/NDF	NDF	$< \tau >$ (ps)
Fe	208.9 ± 4.9	1.18	259	215.7 ± 5.0	1.13	255	212.2 ± 3.5
Cu	193.3 ± 59.8	0.9	66	217.6 ± 86.9	0.9	66	201.1 ± 49.3
Ag	208.0 ± 7.3	0.96	250	210.5 ± 5.8	0.96	234	209.5 ± 4.5
Bi	233.7 ± 72.2	0.93	21	211.8 ± 58.8	1.18	21	220.5 ± 45.6

lifetimes of specific hypernuclei. They are statistical averages of lifetimes for a range of hyperfragments. Their masses, Z and A could not be determined.

Taking the Bi nuclei as example, the fission probability is known to be more than two orders of magnitude higher than that for medium heavy nuclei, such as Fe. Binary fission is the dominant fission mode. The mass of fragments has a Gaussian distribution and the mean nucleon number, A, is about 100 with a width of $\sigma \approx 30$ [31]. Since the hypernuclear lifetime was measured by the time zero difference between the two coincident fragments, it can be assumed that the photo-produced Λ couples with one of the two fragments to form a lighter (medium heavy) but more stable hypernucleus that then decays weakly. Based on this known feature of Bi fission, the measured lifetime is likely an average from the hypernuclei from a $\pm 1\sigma$ mass range of A from $\sim$70 to $\sim$130.

Similarly, lifetime measured from each of the other three lighter targets should be also considered as an average over a range of mass with respect to a mean around 50% of the target A. Thus, strictly speaking, this experiment has measured average hypernuclear lifetime for four different mass regions while the regions from the Fe and Cu target measurements should have a large overlap.

The measured lifetimes (the last column in Table 7) from this experiment are compared in Fig. 22 to those measured by early counter-type experiments that had positive identification on the produced hypernuclei. The solid blue triangle points are from the KEK experiment while the solid black square points are from other earlier experiments, as discussed in the introduction. The results from this JLab experiment are shown as red open circles. The corresponding average mean masses and ranges, as discussed above, are used. For the experiments using delayed fissions

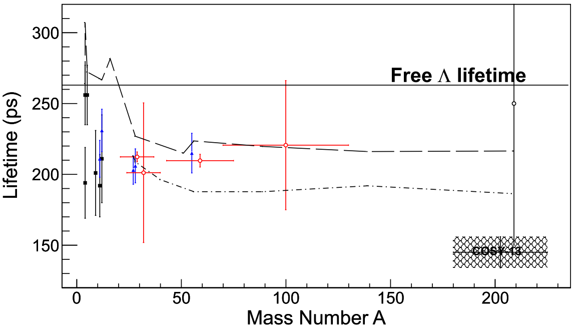

Fig. 22. Comparison of the JLab results (red open circles) that have taken into account the hyper-fragment mass range to the results from counter-type of experiments (blue triangles for the KEK experiment and black square for the earlier other experiments) and to the results from experiments using recoil shadow technique with delayed fission (the published COSY result and a black open circle from the earlier CERN experiment). The two most recent theory calculations are shown as dot–dash [22] and dash [23] lines, respectively.

with the recoil distance method, the COSY result is shown as it was published. The result on Bi from the earlier CERN experiment is shown by a black open circle, while that on U is below the plotting limit and thus not seen in this figure. The two most recent theory calculations are shown as dot–dash [22] and dash [23] lines, respectively, in comparison to the existing experimental data.

A surprising observation is the high production rate of hyper-fragments even from medium heavy nuclei, such as Fe, that were expected to have much lower beam induced fission probabilities. Taking the Fe data as an example. The average of $P_1(N_{p+})$ and $P_1(N_{p-})$ from Table 3 and Table 5 represents dominantly the number of "prompt" fission events including those from primarily produced "cold" hypernuclei that had one-step fission induced by non-mesonic weak decay. The sum of $P_7(N_{d+})$ and $P_7(N_{d-})$ represents the total number of hyper-fragment events. The ratio of hyper-fragment production over the "prompt" fission appears to be about 0.25 (25%). This is quite significant. This ratio remains almost constant up to Ag. In case of Bi, the target energy loss study showed that the one-step fission losses about 5 times more events than the two-step fissions from hyper-fragment production and decay, in comparison to that in case of Fe target. Taking into this account, the above ratio is also the same. This shows that hyper-fragments appear to be the major (if not dominant) decay products from "hot" hypernuclei and are the main sources for the delayed fissions seen in all the lifetime experiments on heavy hypernuclei.

Three additional important aspects were well recognized from features of the obtained results by the technique applied in this experiment. First of all, the technique of using the time difference between the reconstructed time zeros of the two coincident fragments unambiguously separated the type of events. All one-step fission events, photo-fissions and/or weak decay induced fissions from primarily produced "cold" hypernuclei, were gathered within $|T_0| < 0.3$ ns in the time spectrum to form the "prompt" peak. Only the events from weak decay of hyper-fragments with two-step process form the part of decay time spectrum beyond $|T_0| > 0.3$. Therefore, this experiment is able to clearly identify the source of events.

Secondly, the linear feature (in log scale) of the obtained time spectra and the energy loss study indicate that energy loss for low energy heavy nuclei is very significant. Even though the target foils are all thin, most of the hyper-fragments were stopped before decaying weakly. For the primarily produced "cold" hypernuclei that decayed in one-step, they were most likely stopped by energy loss and decayed at rest within the target. On the other hand, energy loss also significantly reduced the number of prompt events from photo fission, since an event will be lost if one of two fragments stopped in the target.

Finally, the lifetime was directly fitted from the time spectrum that was self-aligned. Thus, the results had a small systematic uncertainty, although the results from Cu and Bi targets had significant statistical uncertainties.

8. Conclusion

The unique technique applied in the JLab experiment made it possible to focus on the hyper-fragments that decayed weakly. Their production rate appeared supporting the expected ratio of "cold" over "hot" hypernuclei. This indicates that the lifetime measurement on heavy hypernuclei without a technique that can successfully focus only on "cold" hypernuclei would be "contaminated" largely by decay of hyper-fragments with a range of mass around the mean fragment mass (about 1/2 of the target A). For heavy hypernuclei produced with a higher momentum transfer to the Λ particle, the ratio of "cold" over "hot" hypernuclei would be even smaller so that the hyper-fragments would be more dominantly produced. On the other hand, if heavy hypernuclei were produced with less momentum transfer, this ratio would be significantly higher than that from photo-production. However, the "cold" hypernuclei in this case would not have sufficient energy to escape from the target, thus the loss of "cold" hypernuclei would be severe. Therefore, the hyper-fragments would still be the main products.

For previous experiments using the range technique, the conversion (of distance to time) needs a reliable knowledge of momentum and mass probability functions. Since a large fraction of decayed fissions were from hyper-fragments that were emitted from target just like the "cold" hypernuclei, the mis-assumed mass would cause an incorrect range to time conversion. Secondly, the emission angle of hyper-fragments has wide range. If the range measurement was made by planar device with the assumption that decay hypernuclei were simply along the beam direction, then the distribution of measured positions would be actually a summed range spectrum projected to the beam axis and thus the distribution would not have a good logarithmic shape. Such a strange shape might be mistakenly interpreted as the existence of multiple lifetimes. Both these could be the sources of systematic errors much larger than expected. Therefore, direct decay time measurement is the method to minimize systematic error.

In conclusion, the average lifetimes in the mass regions covered by the different targets are rather consistent around $\sim$200 ps, supporting the expectation of saturation. Although this result cannot exclude unexpected shorter or longer lifetimes for some specific hypernuclei, it at least shows that a systematic decrease in lifetime as hypernuclear mass increases is not a general feature for hypernuclei with masses up to $A \approx 130$. This experiment showed the evidence that decay of hyper-fragments may be the major main source of delayed fissions in all previous experiments studying the lifetime of heavy hypernuclei.

Acknowledgements

The authors would like to thank the support provided by staffs from the Accelerator and Physics divisions at JLab. The work is partially supported by U.S. Department of Energy grants DE-AC05-06OR23177 and DE-FG02-97ER41047. Support was also received from the National Natural Science Foundation of China grants 11175075, 11135002, 11075068 and 11505087 and the State Scholarship Fund program of the China Scholarship Council and the Fundamental Research Funds for the Central Universities lzujbky-2015-71.

References

[1] M. Danysz, J. Pniewski, Bull. Acad. Pol. Sci. III 1 (1953) 42.
[2] M. Danysz, J. Pniewski, Philos. Mag. 44 (1953) 348.
[3] J. Beringer, et al., Particle Data Group, Phys. Rev. D 86 (2012) 010001.
[4] T. Motoba, K. Itonoga, H. Bando, Nucl. Phys. A 489 (1988) 683;
T. Motoba, K. Itonoga, Prog. Theor. Phys. Suppl. 117 (1994) 477;
E. Oset, et al., Prog. Theor. Phys. 117 (1994) 461.
[5] H. Primakoff, W. Chesterton, Phys. Rev. 11 (1953) 1537.
[6] A. Gal, E.V. Hungerford, D.J. Millener, Rev. Mod. Phys. 88 (2016) 035004.
[7] E. Botta, T. Bressani, S. Bufalino, A. Feliciello, Riv. Nuovo Cimento 38 (2015) 387.
[8] R.J. Prem, P.H. Steinberg, Phys. Rev. 136 (1964) B1803.
[9] R.E. Phillips, J. Schneps, Phys. Rev. 180 (1969) 1307.
[10] G. Bohm, J. Klabuch, U. Krecker, F. Wysotzki, Nucl. Phys. B 16 (1970) 46.
[11] Y.W. Kang, N. Kwak, J. Schneps, P.A. Smith, Phys. Rev. 139 (1965) B401.
[12] G. Bohm, et al., Nucl. Phys. B 23 (1970) 93.
[13] R. Grace, et al., Phys. Rev. Lett. 55 (1985) 1055.
[14] J.J. Szymanski, et al., Phys. Rev. C 43 (1991) 849.
[15] H. Outa, et al., Nucl. Phys. A 585 (1995) 109c.
[16] H. Outa, et al., Nucl. Phys. A 639 (1998) 251c.
[17] K.J. Nield, et al., Phys. Rev. C 13 (1976) 1263.
[18] H. Park, et al., Phys. Rev. C 61 (2000) 054004.
[19] D. Jido, E. Oset, J.E. Palomar, Nucl. Phys. A 694 (2001) 525;
A. Parreño, A. Ramos, Phys. Rev. C 65 (2001) 015204;
K. Itonaga, T. Ueda, T. Motoba, Phys. Rev. C 65 (2002) 034617.
[20] K. Sasaki, T. Inoue, M. Oka, Nucl. Phys. A 669 (2000) 331;
K. Sasaki, T. Inoue, M. Oka, Nucl. Phys. A 678 (2000) 455E.
[21] G. Garbarino, A. Parreño, A. Ramos, Phys. Rev. Lett. 91 (2003) 112501;
G. Garbarino, A. Parreño, A. Ramos, Phys. Rev. C 69 (2004) 054603;
C. Chumillas, G. Garbarino, A. Parreño, A. Ramos, Nucl. Phys. A 804 (2008) 162;
E. Bauer, G. Garbarino, A. Parreño, A. Ramos, Nucl. Phys. A 836 (2010) 199.
[22] E. Bauer, G. Garbarino, Phys. Rev. C 81 (2010) 064315.
[23] K. Itonaga, T. Motoba, Prog. Theor. Phys. Suppl. 185 (2010) 252.
[24] T.A. Armstrong, et al., Phys. Rev. C 47 (1993) 1957.
[25] P. Kulessa, W. Cassing, et al., J. Phys. G, Nucl. Part. Phys. 28 (2002) 1715.
[26] H. Ohm, et al., Phys. Rev. C 55 (1997) 3062.
[27] W. Cassing, et al., Eur. Phys. J. A 16 (2003) 549.
[28] O. Hashimoto, S.N. Nakamura, L. Tang, J. Reinhold, et al., 2005, JLab Proposal E05-115.
[29] K. Assamagan, et al., Nucl. Instrum. Methods A 426 (1999) 405.
[30] L. Tang, et al., Phys. Rev. C 90 (2014) 034320.
[31] R.J. Peterson, et al., Z. Phys. A 352 (1995) 181.
[32] F. James, Statistical Method in Experimental Physics, 2nd ed., World Scientific, Singapore, 2006.
[33] F. James, MINUIT Function Minimization and Error Analysis: Reference Manual Version 94.1, 1994, CERN-D-506.
[34] T. Gogami, et al., Phys. Rev. C 94 (2016) 021302 (R);
S.N. Nakamura, et al., Phys. Rev. Lett. 110 (2013) 012502.
[35] T. Gogami, et al., Phys. Rev. C 93 (2016) 034314.
[36] Satoshi N. Nakamura, Toshiyuki Gogami, Liguang Tang, in: Proc. 12th Int. Conf. on Hypernuclear and Strange Particle Physics, HYP2015, 2015;
Satoshi N. Nakamura, Toshiyuki Gogami, Liguang Tang, in: JPS Conference Proceedings, vol. 17, 2017, p. 011002.